Two-photon absorption laser induced fluorescence: rate and density-matrix regimes for plasma diagnostics

Gabi Daniel Stancu

Two-photon absorption laser induced fluorescence: rate and density-matrix regimes for plasma diagnostics

Gabi-Daniel Stancu

Laboratoire EM2C, CNRS, CentraleSupélec, Université Paris-Saclay, 3, rue Joliot Curie, 91192 Gif-sur-Yvette cedex, France

Email : gabi-daniel.stancu@centralesupelec.fr

Abstract

Two-photon Absorption Laser Induced Fluorescence (TALIF) technique employing nanosecond lasers is often used to measure space- and time-resolved distributions of key atomic and molecular radicals in reactive environments such as plasmas and combustions. Although the technique was applied for about four decades, particularly in high pressure non-equilibrium plasmas accurate measurements of species densities remain challenging. With atomic oxygen as an example, central aspects of the technique including the role of photon statistics and line profiles on the two-photon absorption rates, selection rules, spatial and temporal resolutions, photolytic and quenching effects, and absolute calibration methods are discussed. Simulations using rate equations which include non-depletion regime, 3-level and 6-level models are compared and criteria for non-saturation regimes are given for low- and high-pressure plasmas. Solutions of the density-matrix model, which include coherent excitation and Stark detuning phenomena, and the rate equation model are compared. The validity criteria for non-depletion and photolytic-free regimes and rate models are given. The nanosecond TALIF quench-free regime at high laser intensities is investigated using the density-matrix model. The two-photon cross-sections for O, H and N atomic radicals and their ratio with Kr and Xe rare gases used for calibrations are revisited and recommendations are proposed. For TALIF applying ultrafast lasers, the appropriate model for the fluorescence probability is discussed.

1. Introduction

The development and optimization of plasma applications require a fundamental understanding of kinetics, dynamics and energy coupling in discharge media. Laser based spectroscopic diagnostics are powerful tools for *in situ* time- and space-resolved plasma property measurements. Key species densities (e.g. electron, radicals), temperatures (e.g. translation, rotation), main reaction channels (e.g. electron and heavy particle kinetics), transport phenomena (e.g. streamer, convection, shock wave) are plasma characteristics that can be probed by spectroscopic techniques in the spectral range UV to Mid-IR.

Atomic radicals such as O, N, H, C, F and Cl are essential species in low-temperature reactive plasmas. For example, in plasma-assisted combustion O and H radicals initiate oxidation pathways and chain-branching processes at low temperatures [1]. Atomic N is important in plasma enhanced GaN film deposition [2] and together with atomic H, they are key players in the ammonia production [3] that is crucial for fertilizer synthesis. In plasma diamond layer deposition H and C radicals are important [4], whereas F and Cl find applicability in plasma etching processes [5].

While for measurements of these radicals in low-pressure post-discharges in the steady state regime, techniques such as the chemical titration can be used, for fast detection in high-pressure transient plasmas (e.g. nanosecond discharges), only spectroscopic based techniques can be employed. A first candidate is the Optical Emission Spectroscopy (OES), which gives easily access to intense spectrally resolved emission lines. However, the OES provides densities of radical excited states. The ground state can be probed by absorption spectroscopic techniques. First excited levels that are accessible by strong dipole transitions for O (76795 cm^{-1}), H (82259 cm^{-1}), N (83284 cm^{-1}), C (60353 cm^{-1}), F (104731 cm^{-1}) and Cl (71958 cm^{-1}) require light sources in the vacuum UV. Hence, vacuum equipment is necessary and moreover, this is unfeasible for open-air plasma diagnostics. Other possibility for absorption techniques is to probe electric dipole forbidden transitions in the visible spectrum. For example, the transition at 636 nm ($^1D_2 \rightarrow {}^3P_1$) was successfully employed for O detection in a large plasma volume and in steady state, using a sensitive CRDS technique [6]. Note that the Einstein coefficient for this transition is only 1.82×10^{-3} Hz, while for the resonant transition at 130.2 nm ($^3S_1 \rightarrow {}^3P_2$) is 3.41×10^{8} Hz [7]. Therefore, extreme sensitivity is required for the absorption diagnostic when employing forbidden transitions. Time-resolved CRDS with resolution down to 50-ns was successfully applied in sub-mm diameter nanosecond discharges [8]. However, this was done only for allowed dipole transitions.

To overcome the vacuum UV limit and to access ground states, two-photon (or multi-photon) absorption-based techniques were developed. The two-photon absorption was theoretically introduced by Göppert-Mayer [9] and becomes a spectroscopic fluorescence tool after lasers were invented [10] with Doppler-free capabilities [11]. TALIF detections of a couple of atomic and molecular species were performed already in the eighties in flow discharges and flames [12],[13]. Other diagnostic derivates based on two-photon absorption were developed later. This includes two-photon absorption laser induced stimulated emission (TALISE) [14], two-photon absorption laser induced grating spectroscopy (TALIGS) [15] and two-photon absorption laser induced polarization spectroscopy [16] (TALIPS). More recently, TALIF technique was widely used to investigate a large number of plasmas using ns lasers [17][18][19][20][21][22][23][24] and ultrashort lasers [25][26][27].

Despite the numerous applications of the ns-TALIF technique, accurate measurements of species densities remain very challenging, particularly in high pressure transient non-equilibrium plasmas. Investigations of sub-mm plasmas such as streamer discharges at atmospheric pressure requires beam waists down to 10 μm and time resolution below 1 ns. Yet, a strongly focused beam results in a very high instantaneous laser intensity, which can reach 100 $GWcm^{-2}$ even for commercial ns-lasers with energies in the range of 1 mJ per pulse. In saturation regimes, especially when the collisional quenching dominates largely fluorescence processes and it can repopulate ground states, the rate equation models have to be reconsidered. At very high intensity (> 1 $GWcm^{-2}$) rate equation models fail to correctly describe the fluorescence probability and they should be replaced by density matrix models, which include coherent excitation and Stark detuning of transitions under intense laser beams.

Nowadays, ultrashort lasers (e.g. ps, fs), become commercially available and are increasingly employed in plasma laboratories. The so-called mode-locked lasers have very distinctive features compared to the classical ns lasers. These lasers can reach extreme peak intensities (~ 1 $PWcm^{-2}$), large spectral widths (~ 10^2 cm^{-1}) with photon statistics specific to perfect mode-locked lasers. These properties question the validity of rate equation models and calibration methods.

In this article, we revisited the fundamental characteristics of the TALIF technique, the validity of rate equations, the two-photon cross-sections and the calibration schemes. The article is organized in four sections and ends with conclusions. In section 2, the principle and the key aspects of the TALIF technique including selection rules, spatial and temporal resolutions, photon statistics and line profiles, and their effects on the two-photon absorption

rates are presented. In section 3, simulations using rate equations for non-depletion regime, 3-level and 6-level models are compared and criteria for non-saturation regimes are given for low- and high-pressure plasmas. Calibration methods, photolytic and quenching effects are also discussed here. In section 4, solutions of the density-matrix model for significant and negligible quenching are presented and a comparison with the rate equation model is performed. In section 5, the two-photon cross-sections for O, H and N and their ratio with Kr and Xe gases used for calibration, were revisited and recommendations were proposed. The appropriate fluorescence probability model for TALIF using ultrafast lasers is also debated.

2. TALIF principle and key aspects

The principle of the TALIF technique is described as follows. An atom or a molecule can absorb simultaneously two photons if their combined energies correspond to the gap between the ground and the excited state, if they arrive within the atom volume at the same time and if the transition selection rules are fulfilled. The population of excited states pumped by the two-photon absorption process decays in one or more spontaneous emission channels. One of the spontaneous transitions, called the fluorescence channel, is monitored (e.g. see figures 1a, 1b, O transition at 845 nm, Xe transition at 835 nm) using a spectrometer or a photomultiplier (or an ICCD camera) equipped with a narrow band spectral filter that is centered at the fluorescence wavelength. The fluorescence intensity is proportional to the ground state population. Therefore, its measurement determines the atomic or molecular radical density produced, for instance, by plasmas.

2.1 Selection rules

Concerning selection rules, the peculiarity of the two-photon transitions is that it links states with the same parity (even→even or odd →odd states). Transitions such s→s, s→d or $2p^3$→ $2p^23p$ are allowed. In addition, it is possible to select the accessible upper state by a proper choice of the laser polarization. If the two photons are absorbed from a linear polarized laser (two π photons), the transitions are restricted only to $\Delta M_J=0$, while absorption of two photons with the same circular polarization (two σ^+ or two σ^- photons) will lead to transitions only to $\Delta M_J=\pm 2$ in order to conserve the angular momentum of the system [28]. For example, in figure 1a is shown the atomic O level system for two-photon transitions. Only the transition $^3P_0$→$^3P_0$ (for *ΔJ=0)* is represented. This transition has no $\Delta M_J=\pm 2$ channels and only $\Delta M_J=0$ is allowed. Therefore, this transition can be excited by a linear polarized laser beam (π photons) or by two laser beams with left and right circular polarizations (σ^+ and σ^- photons),

but not by a single beam with one circular polarization. We should note that in order to excite only the $^3P_0 \rightarrow {}^3P_0$ transition, the laser spectral width needs to be small compared to the triplet energy separation (i.e. smaller than 0.1 cm^{-1}), otherwise $^3P_0 \rightarrow {}^3P_{2,1}$ transitions are also excited.

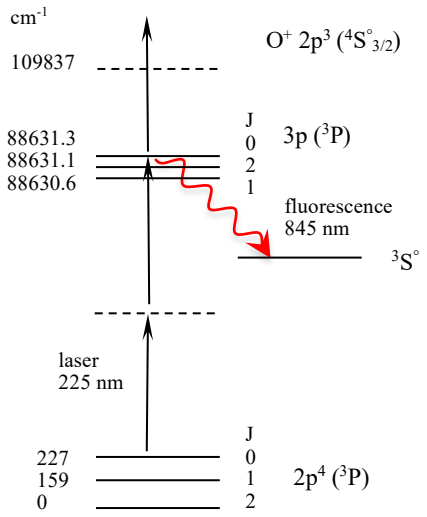

Figure 1a: Atomic oxygen level system for two-photon absorption diagnostics. Only the transition $^3P_0 \rightarrow {}^3P_0$ is shown.

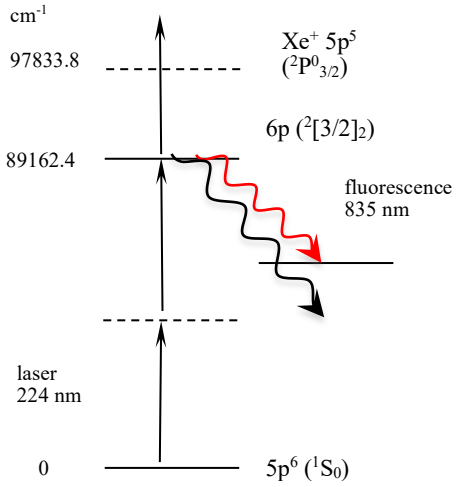

Figure 1b: Xenon level system for two-photon absorption diagnostics. Several fluorescence channels are allowed.

2.2 Spatial resolution

TALIF techniques can provide space-resolved measurements down to μm scale. The spatial resolution of the method is controlled by the laser beam waist and the optical collection system. The beam waist determines the volume in which the fluorescence occurs. Optics can be designed to collect photons from a part or the total fluorescence volume within a certain solid angle.

Commercial lasers have the typical output close to the TEM_{00} mode, so with power P distributed in Gaussian profiles. The intensity (units W/m^2) of a focused laser beam is given by: $I(r,z) = 2P/\pi w(z)^2 \exp\left\{-2\left[r/w(z)\right]^2\right\}$, with $w(z)$ the beam waist (i.e. the beam half width where intensity is I/e^2) in a plane perpendicular to the propagation direction at a given z, r the radial coordinate, and the $w(z)^2 = w_0^2\left[1+\left(z/L_R\right)^2\right]$, where w_0 is the minimum waist (the waist at the focal point), $L_R = \pi w_0^2/\lambda$ is the Rayleigh length (i.e. the length where $w(L_R) = \sqrt{2}w_0$) and λ the laser wavelength. For a lens with focal length, f, much larger than the laser waist at the lens location, w_{lens}, the minimum waist can be calculated by,

$w_0 \approx f\,\lambda/\pi\; w_{lens}$. For example, a gaussian UV laser beam at 225 nm with output diameter of 4 mm and focused by f = 350 mm lens will have a minimum waist of 12.5 μm, while at 3 cm from the focal point the waist will be about 172 μm.

For negligible depletion of the ground state (see later) the fluorescence signal is proportional to $\int_z\int_r I(r,z)^2 2\pi r\,dr\,dz$. Thus, focusing the laser with short optics (w_0 decreases → $I(r,z)$ increases) will increase the fluorescence signal. The double integral for $r \in (0,\infty)$ and $z \in (-\Phi/2,\ \Phi/2)$ is $\int_z\int_r I(r,z)^2 2\pi r\,dr\,dz = \left(2P^2/\lambda\right)\arctan\left(\Phi/2L_R\right)$, where Φ is the z distance from the minimum waist position. From this result we learn that increasing Φ more than twice Rayleigh length makes a small gain in fluorescence signal (50 % of fluorescence signal is within $2L_R$, more than 70 % of fluorescence is collected in $4L_R$). For example, if the collection optics has a magnification one, then Φ equals the slit width of the spectrometer, a fluorescence signal close to maximum is recorded if the laser is focused such as $2L_R \sim \Phi$.

When the spatial region of collection optics (Φ) is much larger than Rayleigh length then the beam waist and Rayleigh length determine the spatial resolution of TALIF technique. If $\Phi < L_R$ then the spatial resolution is determined by the beam waist and collection optics.

2.3 Temporal resolution

The temporal resolution of TALIF technique as for any LIF technique is theoretically determined by the laser temporal pulse width. However, if the detection system (that includes photodiodes, PMT or ICCD cameras) has the response time significantly longer than the usual ns laser pulse width, then it can be unsuitable for measurements of the fluorescence decay time. These measurements are necessary for quenching rate evaluations in high pressure plasmas (see section 3.4). For accurate measurements, the laser pulse duration and the detection resolution should be at least ten times shorter than the characteristic time of the fluorescence signal. When characteristic times are comparable deconvolution techniques may be applied for systems very stable over time. Note that the quenching characteristics time can be ns or hundreds of ps for plasmas at atmospheric pressures. The photodiodes, PMTs and ICCDs have typically the response time down to hundreds of ps. For a faster detection, streak cameras can be employed, whereas ultrashort lasers down to fs are now commercially available.

2.4 Two-photon absorption rate

The rate of absorption (units Hz) for the one-photon transition process (represents the absorption probability per unit of time) at resonance is given by $R^{(1)} = \sigma(\nu_0)\left(I/h\nu\right)$, where $\sigma(\nu_0)$ is the absorption cross-section (units cm^2), I is the laser intensity (units Wcm^{-2}) and $h\nu$ is the laser photon energy (units J). The rate of absorption of the two-photon transition at resonance is given by $R^{(2)} = \sigma^{(2)}(\nu_0)\left(I/h\nu\right)^2$, where $\sigma^{(2)}(\nu_0)$ is the two-photon absorption cross-section (units cm^4s).

For example, for a monochromatic laser intensity of 10 MW/cm^2 and the atomic oxygen absorption profile that is Doppler broadened at 300 K, the Einstein coefficient (3.41×10^8 Hz [7]) for transition $^3P_2 \rightarrow {}^3S_1$ at λ_0 =130.2 nm can be converted in $\sigma^{(1)}(\nu_0) = 1.83\times10^{-13}$ cm^2 that gives $R^{(1)} = 1.20\text{x}10^{12}$Hz. For the unresolved two-photon transition $^3P_2 \rightarrow {}^3P_{2,1,0}$ at λ_0 = 225.6 nm the $\int \sigma^{(2)}\left(\omega\right) d\omega = 2.66\times10^{-35}\text{cm}^4$ (includes $G^{(2)}$=2, see next section) [29] can be converted to $\sigma^{(2)}(\nu_0) = 4.84\times10^{-46}\text{cm}^4\text{s}$ that gives $R^{(2)} = 6.24\text{x}10^4$ Hz. Although the two-photon absorption is much less probable than the one-photon absorption, fluorescence signals are easily detectible. Monitoring fluorescence signals are preferred instead of absorption measurements, because is much simpler to measure a few emitted monochromatic photons in a weak background of radiation than a few absorbed photons from an intense laser. Molar fraction sensitivities down to *ppm* can be easily achieved by TALIF techniques. Another key advantage is that fluorescence techniques provide space-resolved measurements, whereas absorption techniques give line-of-sight integrated signals.

2.5 Photon statistics

The one-photon absorption rate depends on the instantaneous intensity *I(t)* of the laser. The average absorption rate, $\left\langle R(t)\right\rangle$, in the time window that is determined by the temporal resolution of the detection system is $\left\langle R(t)\right\rangle = \sigma(\nu)/h\nu \left\langle I(t)\right\rangle$ and equals the rate one computes using a laser of a constant intensity *I*, where $I = \left\langle I(t)\right\rangle$. This is true whatever the time distribution of the *I(t)*.

In case of the two-photon absorption, the rate is proportional to the instantaneous $I(t)^2$. The average rate in the time window of the detection system is $\left\langle R(t)\right\rangle = \sigma^{(2)}(\nu)\Big/\left(h\nu\right)^2 \left\langle I(t)^2\right\rangle$. Note that this rate can be very different than the rate $R = \sigma^{(2)}(\nu)\Big/\left(h\nu\right)^2 I^2$, computed when using a laser with constant intensity *I*, where $I = \left\langle I(t)\right\rangle$. This is because $\left\langle I(t)^2\right\rangle \geq \left\langle I(t)\right\rangle^2$.

Classical Nd:YAG or dye ns-lasers are commonly multimode with stochastic phase fluctuations. Therefore, the laser output leads to mode beating and intensity fluctuations, which are on the time scale of the reciprocal laser linewidth. For example, if the laser width is 1 cm^{-1}, the time scale is a few ps. The two-photon absorption rate using ns-lasers is enhanced when compared to a CW single mode laser. This because the absorption during intensity maxima outweighs the lower absorption during intensity minima in a pulsed ns-laser. When one measures with a fast photodiode (response time down to hundreds of ps) and fast electronics (~ GHz band width), the intensity of a 10-ns laser represents the averaged value $\langle I(t)\rangle$, in the time window of about 1 ns or less and not the instantaneous laser intensity, *I(t)*. So, from measurements we can compute $\langle I(t)\rangle_{1ns}^2$ as a function of time. However, the average rate, $\langle R(t)\rangle = \sigma^{(2)}(\nu)/(h\nu)^2 \langle I(t)^2\rangle$, depends on the $\langle I(t)^2\rangle$. This last term can be calculated by [30]: $\langle I(t)^2\rangle = G^{(2)}(0)\langle I(t)\rangle^2$, where $G^{(2)}(0)$ is the second order correlation function at time zero, which accounts for photon statistics. This is $G^{(2)}=1$ for a single-mode laser (purely coherent state), $G^{(2)}=2$ for a chaotic multimode laser field, or higher for partially mode-locked lasers ($G^{(2)}\geq 2$). For ns Nd:YAG - dye lasers where the UV light is generated by sum of frequencies, this can be higher than 2 as shown in reference [31]. Thus, the sensitivity of two-photon absorption can be significantly improved when using partially or perfectly mode-locked lasers. Large errors will result on species density or on cross-section measurements if this parameter is ignored.

The second order correlation function at time zero can be measured by splitting the laser beam in two parts and performing photon-coincidence or autocorrelation experiments at zero delay-time between the two beams [30]. However, this parameter is canceled out if a calibration scheme using TALIF with rare gases is employed (see section 3.2). Note that photon statistics are also important for other multi-photon techniques, such as Resonance-Enhanced Multi-Photon Ionization (REMPI) or Coherent Anti-Stokes Raman Spectroscopy (CARS) [31].

2.6 Two-photon excitation line profile

The two-photon absorption spectral cross-section can be computed as, $\sigma^{(2)}(\nu) = \sigma^{(2)} g(\nu)$, where $g(\nu)$ is the value of the two-photon profile function at frequency ν that is the central frequency of the laser, and $\sigma^{(2)}$ is the spectral integrated cross-section. The measured two-photon absorption spectral profile, $g(\nu)$, contains contributions from plasma homogeneous (e.g. collisional, Stark) and inhomogeneous (e.g. Doppler) broadening mechanisms and from

natural and laser broadening mechanisms. The spectral function is the normalized double convolution: $g(\nu) = f_{abs} \otimes f_{laser} \otimes f_{laser}$, where f_{abs} and f_{laser} are the absorption and laser spectral profiles and $\int_{line} g(\nu)\, d\nu = 1$. When laser and absorption profiles are Gaussian, the convolution is also a Gaussian function with $FWHM = \sqrt{\Delta\nu_{abs}^2 + 2\Delta\nu_{laser}^2}$. In case the laser is spectrally much broader than the absorption feature, the Gaussian profile will have $FWHM = \sqrt{2}\Delta\nu_{laser}$.

In figures 2a and 2b, the 845-line and 835-line spectrally integrated fluorescence signals that were time-integrated and normalized to the laser $\int I^2\, dt$ are plotted function of the two-photon wavenumber for O and Xe, respectively [32]. The normalization by the $\int I^2\, dt$ is performed because the laser intensity is usually not constant and changes significantly from pulse to pulse or on a longer timescale, depending on the laser system. As shown in figure 2a, the triplet structure of O atoms due to transitions $^3P_2 \rightarrow {}^3P_{2,1,0}$ measured in a nanosecond air plasma at 1 bar is unresolved. We observe a slight asymmetry of the profile.

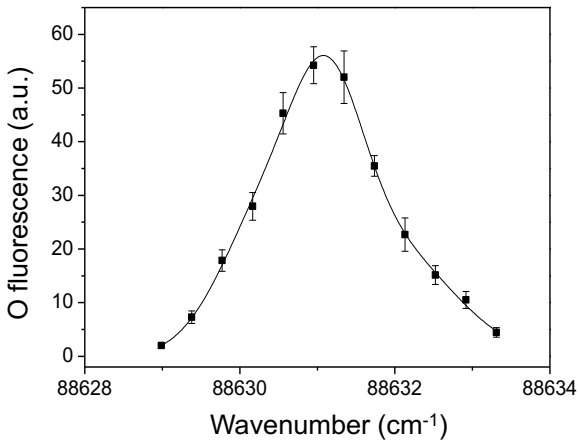

Figure 2a: Oxygen fluorescence function of two-photon wavenumber.

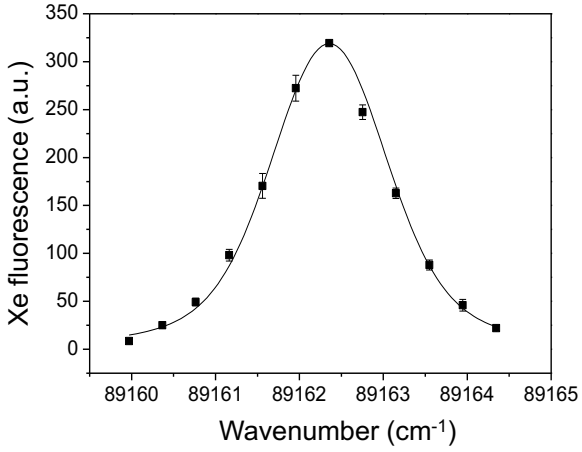

Figure 2b: Xenon fluorescence function of two-photon wavenumber.

Despite that Xe measurements were done in a low-pressure cell at 12 torr and O in a nanosecond discharge at atmospheric pressure, O and Xe profiles show both a FWHM of about 1.7 cm^{-1}, indicating that the laser broadening is the main mechanism. If a Gaussian profile is assumed (this is clearly shown by the fit of the Xe single component) then the laser FWHM is about 1.2 cm^{-1}. Here $g(\nu_{peak})$ for O and Xe being about the same. However, if we employ a 0.1-cm^{-1} laser width, as the Doppler dominated broadening at 300 K is only 0.274

cm^{-1}, the O triplet resulted from $2p^4(^3P_2)\rightarrow 3p\ (^3P_{2,1,0})$ can be spectrally resolved. This because the peak positions are well separated, i.e. 88630.597 cm^{-1}, 88631.146 cm^{-1} and 88631.303 cm^{-1}, respectively. The spectral cross-section at given ν is $\sigma^{(2)}(\nu)=\sum_{J'}\sigma^{(2)}\left(J'\leftarrow 2\right)\, g_{J'}\left(\nu\right)$, where we sum contributions of three components.

In order to achieve the highest sensitivity, the laser is tuned at resonance and the spectral function is evaluated at peak (resonance). This can be computed from measurements as, $g\left(\nu_{peak}\right)=peak\ value/spectral\ area$. For the calibration purpose the measurement is recommended (see section 3.2). This because $g(\nu_{peak})$ will depend on species transitions, experimental conditions and the laser spectral profile. When convolution profiles are Gaussian or Lorentzian functions, we have $g_G\left(\nu_{peak}\right)\simeq 0.94/\Delta\nu_G$ and $g_L\left(\nu_{peak}\right)\simeq 0.64/\Delta\nu_L$, where $\Delta\nu_G$ and $\Delta\nu_L$ are the Gaussian and Lorentzian FWHM in Hz units, respectively. For instance, Xe profile has FWHM=1.7 cm^{-1}, the corresponding peak value gives, $g_G\left(\nu_{peak}\right)=1.84\times 10^{-11}s$.

3. Rate equation regime

In order to obtain the ground state density of an atomic species a kinetic model that includes main processes needs to be employed. When the laser electric field is relatively low and does not perturb atom eigen states and decoherence processes dominate (e.g. collisions, Doppler effect, laser stochastic phase fluctuations) the laser-atom interaction, rate equations can be used to describe the time evolution of population distributions. They can be employed when $\gamma_a+\gamma_L >> \Omega^{(2)}(t), 1/\tau_L$ where γ_a and γ_L are two-photon absorption and laser spectral widths, respectively, $\Omega^{(2)}(t)$ is the composite Rabi frequency and τ_L is the laser pulse duration (see section 4).

Denoting *0, 1, 2* and *i* the ground state, the fluorescence lower state, the fluorescence upper state and the ionization state, respectively (e.g. in figure 2a, for O atom we can consider $2p^3P_0$, $^3S^0$, $3p^3P_0$ and the ionization continuum, respectively), the population kinetics can be described by rate equations [29],

$$\frac{dn_0}{dt} = -R_{02}(t)n_0 + R_{20}(t)n_2$$
$$\frac{dn_2}{dt} = R_{02}(t)n_0 - \left(A + Q + \Gamma(t) + R_{20}(t)\right)n_2 \qquad (1)$$
$$\frac{dn_i}{dt} = \Gamma(t)n_2$$

where $R_{02}(t)$ is the two-photon absorption rate, $R_{20}(t)$ is the two-photon stimulated emission rate, $A = \sum_k A_{2k}$ is the rate of spontaneous one-photon emission to all possible channels (the sum is for all *k* allowed transitions with Einstein coefficients A_{2k}), Q is the quenching rate, $\Gamma(t) = \sigma^{pi}/h\nu\, I(t)$ is the photo-ionization rate, and σ^{pi} is the photo-ionization cross-section. In system (1) we neglect the two-photon spontaneous emission, the ionization from level 1, the repopulating process of the state 0 from state 1 by spontaneous emission and quenching, and the collisional mixing of the triplet ground state. The probability of spontaneous two-photon emission is very small and therefore cannot compete with the spontaneous one-photon emission or the stimulated two-photon emission. At low laser intensity when depletion of the ground state is negligible (i.e. n_0 is about constant), recoupling processes to the n_0 level can be neglected. Therefore, the system (1) is sufficient to correctly describe TALIF processes.

3.1 Non-depletion regime

From analysis of the system (1), a negligible depletion of n_0 is obtain when $R_{02}\tau_L << 1$. The two-photon absorption rate is computed by $R_{02}(t) = \sigma^{(2)} g(\nu) G^{(2)}(0)\left(I(t)/h\nu\right)^2$. The low intensity regime (non-depletion or non-saturation regime) can be reached by a proper choice of laser characteristics: $I(t)$, $h\nu$, τ_L, $\Delta\nu_L$, and $G^{(2)}(0)$. For instance, a typical Nd:YAG - dye system provides laser output characteristics such as multimode ($G^{(2)}=2$), 6 ns pulse length, Gaussian profile with 1 cm^{-1} spectral width and 1 mJ energy per pulse at 225 nm. The laser broadening dominates in this case Doppler and collisional broadenings for a plasma at 300 K and 1 atm. The two-photon absorption rate for O atom with the laser tuned at peak frequency gives $R_{02}(t) = \sigma^{(2)} g_L(\nu_{peak}) G^{(2)}(0)\left(I(t)/h\nu\right)^2 = 9.38\times10^{-47} cm^4 s \left(I(t)/h\nu\right)^2$, with $\sigma^{(2)}$ from [29]. Using different lenses, the intensity and thus the rate, can be changed orders of magnitude. For example, for a laser output of 4 mm diameter, the depletion of the ground state is negligible, $R_{02}\tau_L \sim 10^{-6}$. When a 350-mm focal lens is used, the laser waist can be down to 12.5 μm and saturation effects become very important at focal point, $R_{02}\tau_L \approx 0.8\times10^3$. If the fluorescence is collected at 3 cm away from the focal point,

$R_{02}\tau_L \approx 0.02$. Thus, at this later location we will have a negligible ground state depletion. When using lasers with high spectral purity, due to *g(ν)* enhancement, the saturation is present even for lower pulse energies.

The number of fluorescence photons emitted per unit volume by time *t* is,

$$n_{fluorescence}(t) = \int_0^t A_{21} n_2(t')\, dt' \tag{2}$$

where A_{21} is the Einstein coefficient of the measured fluorescence channel.

For simplicity, if we consider the laser temporal profile being a squared pulse of duration τ_L, after integrating Eq (1) under the assumption of non-depletion regime, we get the fluorescence probability per atom as,

$$\frac{n_{fluorescence}}{n_0} = \frac{A_{21}R_{02}}{\left(R_{20}+\Gamma+Q+A\right)^2}\left[e^{-\left(R_{20}+\Gamma+Q+A\right)\tau_L} + \left(R_{20}+\Gamma+Q+A\right)\tau_L - 1\right] + \frac{A_{21}R_{02}}{\left(R_{20}+\Gamma+Q+A\right)\left(Q+A\right)}\left[1 - e^{-\left(R_{20}+\Gamma+Q+A\right)\tau_L}\right]. \tag{3}$$

The total number density of fluorescence atoms induced by one laser pulse can be obtained from (3) for any laser pulse shape as,

$$n_{fluorescence} = n_0\left(\frac{A_{21}}{Q+A}\right)\frac{\sigma^{(2)}g(\nu)}{\left(h\nu\right)^2}G^{(2)}(0)\int_0^\infty I^2(t)\, dt. \tag{4}$$

Equation (4) is the literature commonly used expression for plasma diagnostics. However, this expression is valid if the following requirements are satisfied:

(i) $\tau_L R_{02} << 1$, this condition implies the negligible depletion of the ground state; the laser pulse is much shorter than the characteristic time of the two-photon absorption process ($\tau_L << 1/R_{02}$),

(ii) $R_{20}+\Gamma << A+Q$, two-photon stimulated emission and ionization rates are much smaller than fluorescence and quenching rates.

In figure 3a and 3b, examples of fluorescence measurements for atomic oxygen and xenon as function of $\int I^2(t)\, dt$ are presented [32]. Measurements were performed with a 6-ns laser for intensities below 200 MW/cm^2 in a nanosecond pulsed discharge for O at atmospheric pressure and in a reference gas cell for Xe at 12 torr. The 1-mJ energy per pulse was focused by a 35-cm UV lens and the beam diameter at the measurement location was about 350 μm. The two criteria $\tau_L R_{02} << 1$ and $R_{20}+\Gamma << A+Q$ are theoretically fulfilled and thus

measurements should be in the non-depletion regime. Indeed, this regime is shown in figures 3a and 3b by linear dependencies of time-integrated fluorescence signals as function of laser time-integrated squared intensities. Note that if we compute $\ln\left(I_{LIF(1)}/I_{LIF(2)}\right)/\ln\left[\left(I_{(1)}/I_{(2)}\right)\right]$ for both figures, where (1) and (2) are any point pairs of linear fits, a value of about 2 is obtained. Therefore, Eq (4) is valid for the density calculation. Note that when the saturation process occurs, the slope becomes smaller than 2, whereas when photolytic processes are present the slope becomes larger than 2 (see 3.3 section).

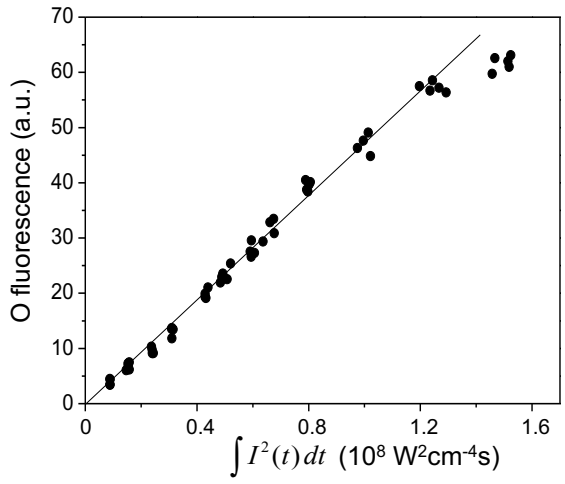

Figure 3a: Oxygen fluorescence function of time integrated I^2.

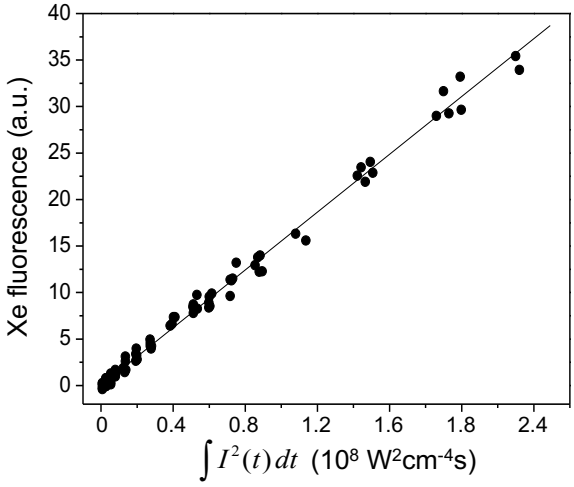

Figure 3b: Xenon fluorescence function of time integrated I^2.

3.2 Calibration using rare gases

Equation (4) gives the time integrated number density of fluorescence atoms, which is proportional with the ground state number density (n_0), and laser and atom properties. In experiments, the recorder fluorescence signal is the result of the integration of $n_{fluorescence}$ over the fluorescence collection volume and the detection solid angle. In addition, the transmission of the optical system and the quantum efficiency of the detector will determine the amplitude of the recorded signal. The fluorescence signal is given then by, $S_F = D(\lambda)\, h\nu_F\, \Omega/4\pi \int_V n_{fluorescence}\, dV$, where $h\nu_F$ is the energy of fluorescence photons, $D(\lambda)$ accounts for transmission and quantum efficiency of the detector at the fluorescence wavelength. Here, we assumed an isotropic fluorescence and all locations from the fluorescence volume are collected with about the same solid angle Ω, which represents a fraction of 4π sr.

As for OES [33], the absolute calibration of the detection spectral response can be done using standard radiance lamps (e.g. tungsten), usually opaque grey bodies (i.e. spectral emissivity is constant) for which the absolute spectral radiance is known (units W/ nm m^2 sr). However, space- and time-distributions of fluorescence atoms and the solid angle changes have to be considered when compared to a standard radiance lamp that is usually a steady state surface source.

An improved calibration scheme is to employ Rayleigh or spontaneous Raman scattering methods [34]. Scattering measurements are performed in a reference gas cell filled with a known gas density (e.g. H_2) for which scattering cross-sections are known. Using the same detection system, optical and spectral calibration parameters can be determined. However, as the Rayleigh or spontaneous Raman signals depends linearly on the laser intensity, while the TALIF signal is proportional to the square of the laser intensity and photon statistics, the calibration is not entirely resolved. The second order correlation function and spatial distributions need be evaluated.

The most common method, which accounts for laser properties, namely spatial, spectral and temporal intensity profiles, and photon statistics is the employment of TALIF signals recorded in a reference gas cell, which is filled with known Xe or Kr gas densities [35],[36],[37]. For example, the calibration using Xe has the advantage of very similar two-photon absorption and fluorescence transitions compared to O atom (see figure 1). The same laser set-up with a small wavelength tuning can scan both species and therefore the same spectral, temporal and spatial profile, and photon statistics of the laser can be considered. The fluorescence signal being spectrally close, the detector sensitivity is usually about the same. In this case the oxygen density in the ground state (e.g. the $^3P_2$ state) is given by,

$$n_O = \frac{\left(\frac{A_{21}}{A+Q}\right)_{Xe}}{\left(\frac{A_{21}}{A+Q}\right)_{O}} \frac{\sigma^{(2)}{}_{Xe}}{\sigma^{(2)}{}_{O}} \frac{g(\nu_{peak})_{Xe}}{g(\nu_{peak})_{O}} \frac{S_{F_O}(\nu_{peak})}{S_{F_{Xe}}(\nu_{peak})} n_{Xe} \qquad (5)$$

where the time- and spectral-integrated fluorescence signals (S_F) are measured at the resonance wavelength (at peak) for the two-photon transitions and are normalized to $\int I^2\, dt$. Eq (5) should include the ratio of D terms and photon energies if fluorescence signals and two-photon absorptions are at very different wavelengths.

We should note that the radical density obtained based on Eq (5), requires knowledge of the quenching (see section 3.4) and of the spectroscopic data, which are given in spectroscopic

databases and journals. However, in particular for radicals, two-photon absorption cross-sections are sparsely found in the literature. The cross-section measurement requires knowledge of the radical density, which is done by other techniques, such as chemical titrations in gas flow systems [35] or using quench-based methods [18].

3.3. Photolytic effects

Photolytic phenomena are observed in TALIF experiments performed using ns-lasers [25][38][39]. For example, in oxygen containing plasmas, photodissociation of ozone or molecular oxygen due to the laser intensity at 225 nm, may occur at important rates. The photon energy, i.e. 5.5 eV, exceeds the bond energies and the photodissociation of O_2 and O_3 occurs via Herzberg continuum and Hartley bands, respectively [40]. Atomic hydrogen detection by TALIF suffers as well from photolytic interferences [38]. H atoms are additionally produced by photodissociation of hydrocarbons or water vapors by a UV beam at 205 nm, which is typically employed for H-TALIF. Nitrogen molecules cannot be photo-dissociated by 210 nm or 206 nm UV beams that are usually used for N-TALIF. However, other plasma molecular components containing nitrogen (e.g. ammonia) may induce photolytic effects.

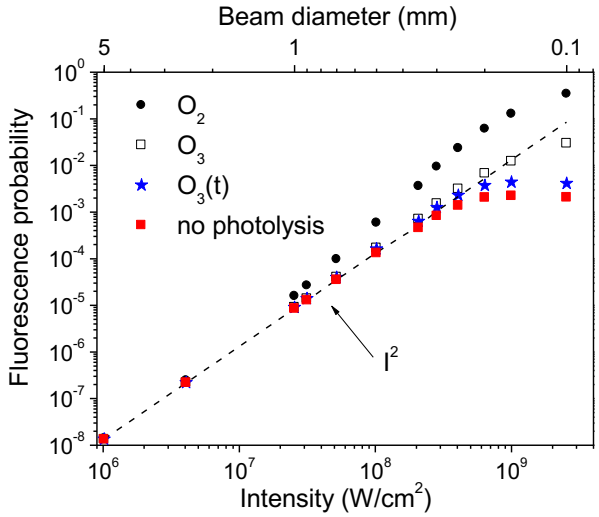

Figure 4. Fluorescence probability function of laser intensity for: no photolysis (full squares), dashed line (Eq 4), photolysis of O_2 (circles), photolysis of O_3 (empty squares) and $O_3(t)$ (stars).

In figure 4 simulations of the fluorescence probability function of the laser intensity were made for O-TALIF. The beam diameter is calculated assuming a uniform beam of a 10-ns

laser with 2 mJ energy per pulse. The laser width is considered 0.1 cm^{-1} for absorption rate calculations and the quenching frequency is assumed 10^{10}Hz. The spectroscopic data were taken from [7],[34]. In case of the negligible photolysis, the fluorescence probability was computed using Eq (1) (full squares) and Eq (4) (dashed line). The two curves are in excellent agreement below 300 $MWcm^{-2}$. At higher intensities the saturation occurs (significant depletion of ground state) and Eq (4) overestimates the fluorescence probability. In case of the molar ratio $[O]/[O_2]= 10^{-6}$, the fluorescence probability was calculated by adding the O production term $2\sigma_{O_2}^{ph}\left(I/h\nu\right)\left[O_2\right]$in Eq (1), with $\sigma_{O_2}^{ph}=3\times10^{-24}cm^2$ taken from [40]. The fluorescence probability is represented with circles. These simulations were performed using O_2 density constant during the photolytic time (i.e. τ_L). This assumption is easily justified by computing the photo-dissociated fraction of O_2, which is negligible for a 10-ns pulse and for the entire range of intensities shown here ($R_{O_2}^{Ph}\tau_L << 1$).

Note that in the non-depletion regime (I < 300 $MWcm^{-2}$), the fluorescence signal scales with the intensity at powers larger than two. For comparison, the dashed line corresponds to a slope of 2. In case of saturation regime (I > 300 $MWcm^{-2}$), where the slope should be normally less than two (as shown by full squares), the photolytic phenomenon increases the fluorescence power dependence and can compensate the slope decrease due to the power saturation. For example, if measurements are performed for intensities from 400 MW cm^{-2} to 1 $GWcm^{-2}$ the slope will be about 2, i.e. the same as for dashed line, which falsely justify the non-depletion regime. The use of Eq (4) in this case overestimates the O density in plasma by more than one order of magnitude. However, for large atomic density, e.g. when O represents 0.1 % of O_2 or more, the photolytic effect will be negligible for laser intensities considered here.

Simulations were performed also for the photolysis of O_3 that was consider at the same initial density as atomic oxygen. Because a constant O_3 is not justified for all intensities, calculations were performed for the time-depend O_3(t) (stars), by adding a specific O_3 differential equation in Eq (1) and for the constant O_3 during the photolytic time (empty squares), by adding the O production term $\sigma_{O_3}^{ph}\left(I/h\nu\right)\left[O_3\right]$ in Eq (1). The photolytic cross-section was taken as $\sigma_{O_3}^{ph}=3.2\times10^{-18}cm^2$, with a yield of 0.15 % for O(^{3}P) at room temperature plasmas [41]. The first case is when the plasma ozone production does not compensate the O_3 photodissociation process during τ_L. The second case represents a plasma which maintains the ozone density during the laser pulse because of very high production rates. As shown in figure 4, the

fluorescence probability is largely enhanced at high intensities, in particular when plasma maintains a constant ozone density. Note that, the photolytic effect will be even larger when O_3 is present in larger quantities than O.

Thus, for examples given here the atomic oxygen density is considerably overestimated if these processes are not considered. However, the photolysis phenomena can be avoided. A photolytic process will not impact the fluorescence signal if the number of new created atoms during the laser pulse is negligible compared to the initial number of atoms. For instance, in case of O-TALIF when studying plasmas containing molecular oxygen, the criterion $2\sigma_{O_2}^{ph}\left(I/h\nu\right)\tau_L\left(n_{O_2}/n_O\right)<<1$ should be proven, otherwise the oxygen TALIF signal will be partially produced by the photodissociation of the ozone followed by the two-photon excitation.

We should note also that O(^{3}P) produced by photolysis of O_2 have about 0.15 eV (e.g. 1300 K) translational energy. In case they are produced in quantities comparable or larger than the O density in plasma, the two-photon absorption profile will be enlarged due to the Doppler effect. At low pressures (e.g. 1 mbar) this hot population is not thermalized during the fluorescence acquisition time. As the photolysis fragments fly in opposite directions with velocity distributions on the Newton's sphere [42], the Doppler effect induces a larger broadening of the two-photon absorption profile. Consequently, we expect a profile with FWHM larger than 0.274 cm^{-1}, which corresponds to Doppler broadening at 300 K. However, at atmospheric pressure thermalization happens in time scale below 1 ns. Therefore, the broadening effect will be reduced, in particular if the density of O hot atoms is much less than the total species density. In case of the ozone photodissociation the translation energy available for O(^{3}P) is even larger, so the Doppler enhanced broadening is also expected.

3.4 Quenching at atmospheric and high pressures

i) case of non-depletion regime

In case of the non-depletion regime, the collisional quenching of excited states at atmospheric and high pressures induces a couple of effects. The fluorescence amplitude decreases, is shorter in time and the two-photon absorption rate may decrease ($g(\nu)$ decreases) because of a significant collisional broadening. However, even if the fluorescence probability decreases, the fluorescence signal may be detectable because of large ground state densities in high-pressure plasmas.

The quenching rate depends on the density, the relative speed and the nature of the particle colliding with the atom in the excited state. Measurements of the quenching rate at low

pressure (below 100 mbar) are usually done using Stern-Volmer plots [35][36]. The fluorescence decay is measured using ns-pulsed lasers with time-resolved detection. The measured decay time is given then by, $\tau = \left(\sum_k A_{2k} + Q \right)^{-1}$. In the limit of very low pressure, the measured decay time equals the radiative lifetime, $\tau_{rad} = 1 \Big/ \sum_k A_{2k}$. The quenching rate is given by, $Q = \sum_p k_p n_p$, where k_p (cm^3/s) and n_p (cm^{-3}) are the collider quenching coefficient and density, respectively. Note that the quenching may be also a three-body collision process, particularly in high pressure environments [23][24]. The total quenching rate is then calculated by adding $k_{3p}\,(n_p)^2$ terms, where k_{3p} (cm^6/s) is the three-body quenching coefficient. An example of the fluorescence decay measurement is shown in figure 5. The fluorescence of Xe atoms (transition at 835 nm) is measured in a gas cell at 12 torr. According to NIST [7], the radiative lifetime of the Xe excited state $5p^5(^2P_{1/2})6p\ ^2[3/2]_2$ (89162.4 cm^{-1}) is τ_{rad} = 23 ns, whereas the measured lifetime from the single exponential decay shown in figure 5 is τ_m = 5 ns. Thus, there is a significant quenching for the cell experiment. This gives a quenching coefficient for Xe of about 4 x$10^{-10}$$cm^3$/s, which is in good agreement with the literature [37].

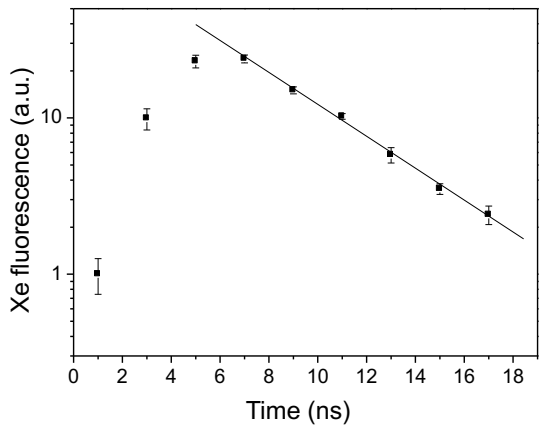

Figure 5: Time evolution of Xe fluorescence line at 835 nm.

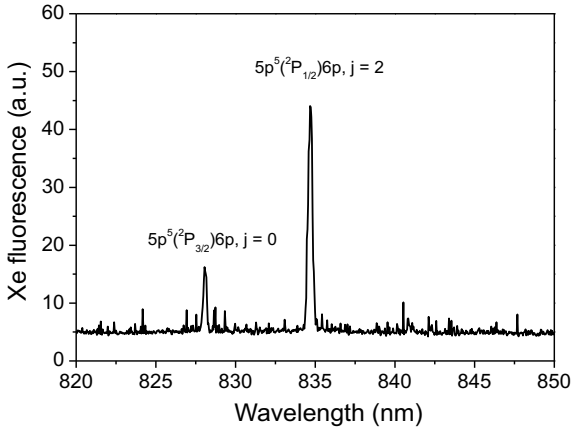

Figure 6: Xe fluorescence spectrum: 835 nm direct pumping; 828 nm pumping by quenching.

In figure 6 the Xe fluorescence spectrum in the range 820 nm to 850 nm is shown. We remark that beside the line at 835 nm a second fluorescence line appears at 828 nm. The upper state $(5p^5(^2P_{3/2})6p\ ^2[1/2]_0)$ of this transition is at 80119 cm^{-1}. However, the two-photon absorption pumps only the level $5p^5(^2P_{1/2})6p\ ^2[3/2]_2$ at 89162 cm^{-1}. Thus, the presence of 828 nm fluorescence line is an example of quenching channels of the Xe $5p^5(^2P_{1/2})6p\ ^2[3/2]_2$ state. Due

to collisions the population transfer occurs, and the quenching induced fluorescence is generated.

The quenching rate for each channel can be obtained if species densities of each channel are measured. However, for the purpose of non-saturated TALIF diagnostics only the total quenching rate is necessary.

In figure 7 the relative fluorescence signal is simulated considering as excitation a laser pulse with a Gaussian temporal profile of 6-ns FWHM. Calculations were done using Eq (4) and assuming total quenching rates of 10^7, 10^8, 10^9 and 10^{10} Hz. The fluorescence amplitude and duration decrease with the increase of the quenching rate. We note that for $Q \geq 10^9$Hz the fluorescence profile has the same width as the $I^2(t)$ profile. Therefore, in this situation the quenching rate cannot be obtained from the measured decay even if the electronics provide a better temporal resolution.

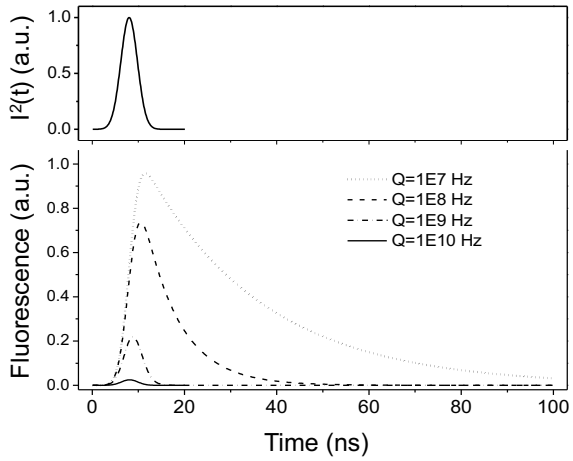

Figure 7: Simulated fluorescence signals function of time for different quenching rates (down). Gaussian I^2 function of time (up).

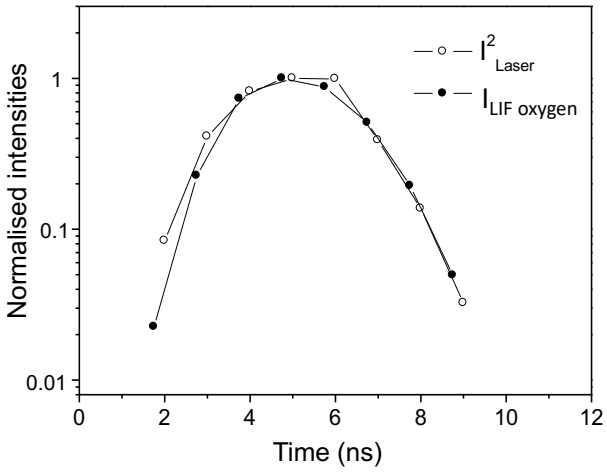

Figure 8: Normalized measured O fluorescence intensity function of time together with normalized laser $I^2(t)$.

An example performed in air plasma at atmospheric pressure is shown in figure 8. The atomic oxygen fluorescence measured by TALIF is plotted function of time together with the laser $I^2(t)$. The fluorescence and laser profiles exhibit a FWHM of about 4 ns. From this measurement we can conclude that the quenching rate is higher than 10^9 Hz. Indeed if we consider quenching coefficients of the O ($3p[^3P_J]$) excited state (e.g. $k_{N2}=5.9\times10^{-10}cm^3s^{-1}$, $k_{O2}=9.3\times10^{-10}cm^3s^{-1}$, $k_{Ar}=2.5\times10^{-11}cm^3s^{-1}$ at 300 K [37]) for the dry air composition (21% O_2; 78%N_2; 1% Ar), quenching rates of 1.6×10^{10}Hz for 300 K and of 8.7×10^9Hz at 1000 K are obtained. The coefficients for 1000 K were scaled with the square root of the temperature,

since the relative velocity between the oxygen atom and the quencher is given by $v_r = \left(8kT/\pi\mu\right)^{0.5}$.

In plasmas and in reactive media in general, the nature, the density and the temperature of colliders can be time- and space-dependent. Therefore, to convert fluorescence signals to absolute or relative densities, knowledge of the quenching rate is needed with temporal and spatial resolutions.

In order to directly measure quenching rates in high pressure discharges, we need to be able to distinguish excitation and quenching processes. The characteristic time of the quenching being usually higher than 100 ps, the excitation using ps or fs lasers is then required [43][44]. The fluorescence signals need to be measured using ultrafast detection such as streak cameras or by pump-probe spectroscopic techniques. Another solution is to perform TALIF in high intensity regimes where the quenching dependence may become negligible (see section 4).

ii) case of significant depletion

In figure 9 we represent the processes one should consider if experiments are done at high pressures and if we have a significant depletion of the ground state (e.g. $R_{02}\tau_L \sim 1$). As the depletion increases, a significant population will return on the ground state ($2p^4(^3P_2)$, 0 cm^{-1}) from the $3p(^3P_J)$ excited state by three parallel processes, i.e. the two-photon stimulated emission, the two-step spontaneous emission and quenching. The two-photon spontaneous emission is also present but at a frequency many orders of magnitude less than other processes. In addition, population transfers from levels $2p^4(^3P_1)$ (159 cm^{-1}) and $2p^4(^3P_0)$ (227 cm^{-1}) will arrive on the ground state $2p^4(^3P_2)$ (0 cm^{-1}).

Besides the levels shown in figure 9, oxygen atom has three intermediate lower levels: $3s(^5S_2)$ at 73768 cm^{-1}, which is coupled radiatively to $3p(^5P)$ by the transition at 777 nm, and to the ground states $2p^4(^3P_J)$, metastables $2p^4(^1S)$ at 33793 cm^{-1} and $2p^4(^1D)$ at 15868 cm^{-1}, respectively. The quenching rates are large for transitions that are radiatively allowed. Thus, the excited states $3p(^3P_J)$ are expected to be efficiently quenched towards $3s(^3S_1)$ (Einstein coefficient ~ 10^7 Hz), and this level, in a second step, towards the ground state (Einstein coefficient ~ 10^8 Hz). The quenching rates towards $3p(^5P)$, $3s(^5S)$, $2p^4(^1S)$, $2p^4(^1D)$ are less important, because it requires the spin change. Dagdigian et al. [45] found that the quenching channel $3p(^3P) \rightarrow 3p(^5P)$, which requires the spin change, compared to the total quenching of $3p(^3P)$ represented 8% and 3%, for O_2 and N_2 collisional species, respectively. Thus, one expects a strong coupling of the excited state $3p(^3P)$ to the ground state by quenching via the intermediate state $3s(^3S)$. In addition, quenching frequencies could be enhanced by the

presence of humidity, high densities of radicals and charge species, or pressure increase due to adiabatic heating [46]. We should note that in a molecular gas the quenching highest value will be limited by the heavy particle collision frequency, which can be computed from the heavy particles mean free path and their thermal speeds. In plasma with high degree of ionization, charge collisions may change this limit.

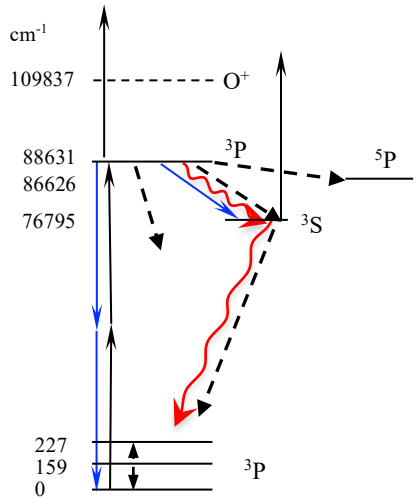

Figure 9. O levels and processes: collisional processes (dashed arrows), spontaneous emissions (red arrows), stimulated emissions (blue arrows), two-photon absorption and ionization (black arrows).

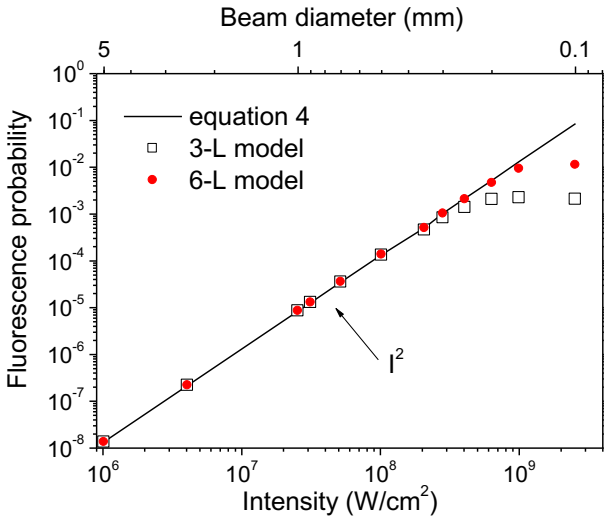

Figure 10. Fluorescence probability calculated function of intensity: no depletion (line), 3-level model (squares) and 6-level model (circles). Beam diameter is computed for 2 mJ energy per pulse.

As discussed above, for a plasma at room temperature at 1 bar containing oxygen, nitrogen or air, the quenching frequency of the $3p(^3P)$ excited states due to O_2 or N_2 can reach 10^{10} Hz. Assuming quenching frequencies up to the order of 10^{10} Hz is realistic for plasmas in gases from low pressure to atmospheric or slightly higher pressures, for channels $3p(^3P) \rightarrow 3s(^3S°)$ and $3s(^3S°) \rightarrow 2p^4(^3P_{2,1,0})$ and for collisional frequencies of population transfers between the ground state triplet components $2p^4(^3P_{2,1,0})$.

The system of equation to be solve should contain at least the following equations:

$$J=2: \quad \frac{dn_{02}}{dt} = -R_{(02)2}(t)n_{02} + R_{2(02)}(t)n_2 - n_{02}(q_{20}+q_{21}) + n_{01}q_{12} + n_{00}q_{02} + n_1\left(A_{1(02)} + Q_{1(02)}\right)$$

$$J=1: \quad \frac{dn_{01}}{dt} = -n_{01}(q_{10}+q_{12}) + n_{02}q_{21} + n_{00}q_{01} + n_1\left(A_{1(01)} + Q_{1(01)}\right)$$

$$J=0:\ \frac{dn_{00}}{dt}=-n_{00}(q_{01}+q_{02})+n_{02}q_{20}+n_{01}q_{10}+n_1\left(A_{1(00)}+Q_{1(00)}\right) \qquad (6)$$

$$\frac{dn_1}{dt}=n_2\left(A_{21}+Q_{21}\right)-n_1\left(A_{1(01)}+Q_{1(01)}+A_{1(00)}+Q_{1(00)}+A_{1(02)}+Q_{1(02)}+\Gamma_{1i}(t)\right)$$

$$\frac{dn_2}{dt}=R_{(02)2}(t)n_0-\left(A_{21}+Q_{21}+\Gamma_{2i}(t)+R_{2(02)}(t)\right)n_2$$

$$\frac{dn_i}{dt}=\Gamma_{2i}(t)n_2+\Gamma_{1i}(t)n_1$$

where n_{02}, n_{01}, and n_{00} are the populations of ground states *J=2*, *J=1* and *J=0*, respectively.

The stimulated one-photon emission at 845 nm may be included in the system. This phenomenon was observed, for instance, in references [14][47][48]. For quantitative description of TALISE signals the stimulated process need to be added in Eq (6). However, this process happens only in the beam direction (i.e. under a very small solid angle) and as shown in [49], it is less important than the spontaneous fluorescence which initiates the phenomenon.

The system (6) was solved considering quenching frequencies $Q_{21}=10^5$, 10^8, 10^9 and 10^{10} Hz, $Q_{1(00)}+Q_{1(01)}+Q_{1(02)}=10^5$, 10^8, 10^9 and 10^{10}Hz, respectively. Ground state collisional frequencies of population transfers, q_{xy}, were also considered on the order of 10^5, 10^8, 10^9 and 10^{10} Hz, respectively and their weights were chosen to obtain the Boltzmann asymptotic distribution at 300 K in case the laser perturbation is removed (namely, fractions 0.742:0.208:0.05). Ionization cross-sections were assumed the same, the laser second order correlation function $G^{2)}(0) = 2$ and the pulse duration $\tau_L = 10$ ns. The two-photon spectral profile function was considered as the double convolution of the laser profile and the absorption profile determined by the Doppler broadening at 300 K. Note that the beam diameter on the top axis in figures 4, 10, 11 and 12 is computed assuming a uniform laser intensity with energy per pulse of 2 mJ. This axis should be ignored in case of lasers with different pulse energies.

In figure 10, the fluorescence probability was calculated for quenching and collisional rates of 10^{10}Hz, assuming laser FWHM=0.1 cm^{-1}, function of laser intensity for non-depletion regime (Eq 4), 3-level (Eq 1) and 6-level (Eq 6) models. We note that below intensities of about 300 MW/cm^2, models and Eq 4 give identical results. Differences are large at higher intensities when the depletion of ground state (n_{02}) becomes important. In case of the 6-level model the slope remains the same even for higher fluxes. This because the quenching coupling processes return significant populations into the ground state. The fluorescence signal continues to

increase and saturates at laser intensities higher than about 800 MW/cm^2. Note that solutions from 3-level and 6-level models are expected to be identical when the ionization rate becomes much larger than the quenching and collisional rates. This can happen for intensities significantly higher than 1 GW/cm^2. However, the validity of rate equations is questionable at very high intensities (see section 4), therefore these simulations were performed below about 2.5 GW/cm^2.

In figure 11 the fluorescence probability was calculated using the 6-level model for quenching and collisional rates of 10^8, 10^9, 10^{10} Hz and 10^5Hz, function of laser intensity and assuming the laser FWHM = 0.1 cm^{-1}. The last value corresponds to negligible quenching (i.e. Q << A, $\leftrightarrow$ Q < 10^6). The lines represent the fluorescence probability per atom calculated using Eq (4), which supposes the non-depletion (non-saturation) regime. At low laser intensities in the non-depletion regime, the fluorescence probability per atom can be more than two orders of magnitude higher in case of low-pressure plasmas (negligible quenching) compared to atmospheric pressure plasmas. This difference is reduced in the saturation regime to a factor 2 at 2.5 GWcm^{-2}.

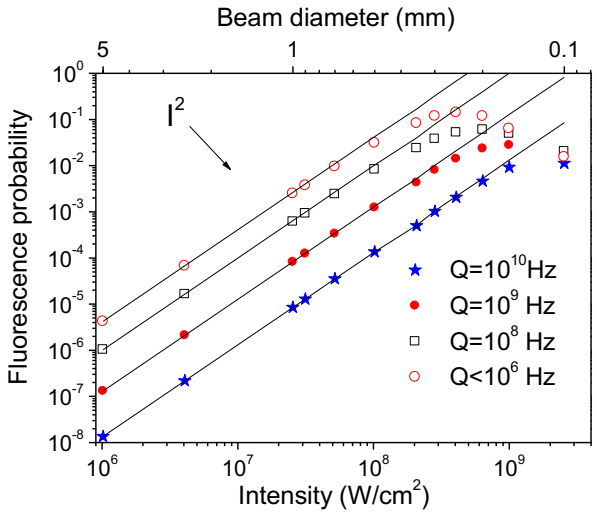

Figure 11. Fluorescence probability calculated function of intensity using the 6-level model for Q=10^{10} Hz (stars), Q=10^9 Hz (full circles), Q=10^8Hz (squares), Q<10^6 Hz (open circles) and corresponding values using Eq 4 (lines).

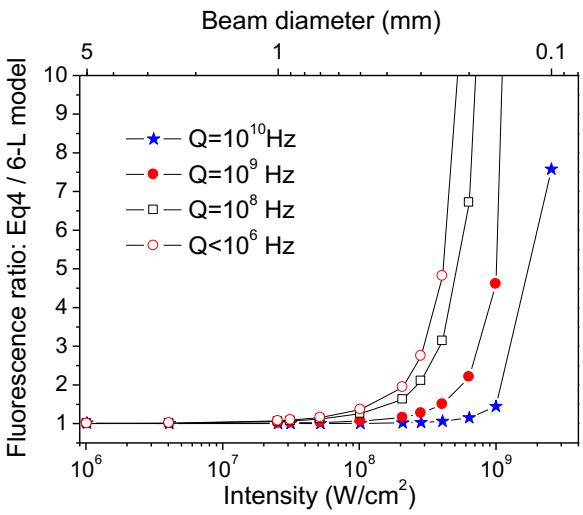

Figure 12. Ratio of fluorescence probabilities calculated using Eq 4 and 6-level model function of laser intensity for quenching frequencies from figure 11. Beam diameter is computed for 2 mJ energy per pulse.

As shown, for instance in [50], for 1-photon induced fluorescence (LIF), the fluorescence signals are less dependent on the quenching rate at high laser intensity. In case of TALIF, this happens because the number of two-photon absorption processes become comparable with the

number of two-photon stimulated emission that refill the ground state, with rates higher than the quenching rate. Therefore, the excited state density becomes comparable with the ground state density. For intensities higher than 1 GWcm^{-2} the TALIF technique becomes less sensitive to quenching and may be used to determine the density of atoms in the ground state in high pressure plasmas [51], where Q is expected to change spatially and temporally in the range of 10^9 Hz to 10^{10} Hz. However, this method will not benefit of the precision of a spectroscopic technique but will be tributary to uncertainties of all collisional rates. In addition, because laser beams have usually Gaussian radial profiles, this results in a non-uniform saturation over the beam cross-section that worsen also the TALIF accuracy. Moreover, as the validity of rate equations is questionable for I > 1GWcm^{-2}, uncertainties larger than a factor two are expected. Note that for O atoms the TALIF precision is limited in the non-depletion regime by: ± 30% for $\sigma^{(2)}$, ± 10% for A, to which we should add about ± 10% for Q, when this is directly measured from the decay time of the excited state.

In figure 12 the ratio of the fluorescence probability computed with Eq (4) and 6-level model is plotted for the same conditions as in figure 11. We can see that Eq (4) overestimates the fluorescence probability (so, the density of the ground state species) when the laser intensity is high. In particular for low pressure plasma (negligible quenching case), one should employ lasers with intensities below 20 MWcm^{-2}. Otherwise the density obtained using Eq (4) can be overestimated from percentage to orders of magnitude (e.g. a factor 10 at 500 MW/cm^2). In case of high collisional plasmas, e.g. Q=10^{10}Hz, Eq (4) works correctly for intensities up to 300 MWcm^{-2}.

In figure 13 the fluorescence probability was calculated for quenching and collisional rates of 10^{10} Hz, function of the laser intensity and assuming the laser FWHM = 0.1 cm^{-1}, 1 cm^{-1}, and 2 cm^{-1}. As expected, the fluorescence probability is smaller for spectrally broader lasers and converges at high intensities when depletion is significant. The fluorescence probability converges to about the same values for I > 1GW/cm^2. This because when the laser intensity exceeds a certain value, the two-photon rates dominate the coupling between ground and excited states, the ratio of their populations becomes constant and equal to the ratio of their statistical weights. This ratio remains constant if we continue to increase the laser intensity. Note that ionization rates are independent on the laser width (bound-free transition). Consequently, the fluorescence probability may become independent of the spectral laser width for intensities significantly higher than 1GW/cm^2.

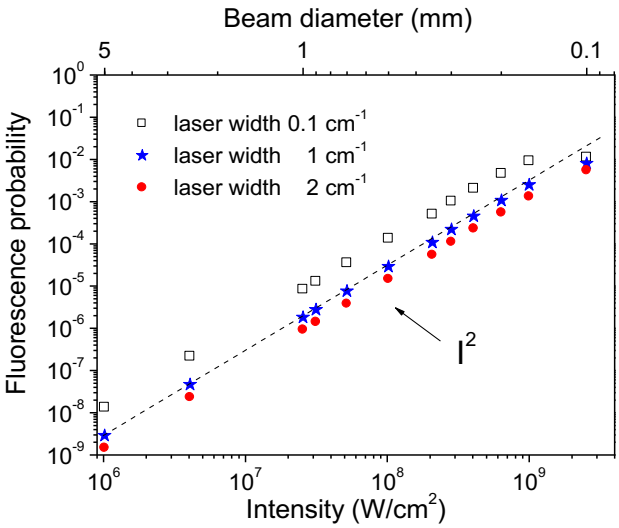

Figure 13. Fluorescence probability calculated function of intensity for laser width 0.1 cm^{-1} (squares), 1 cm^{-1} (stars) and 2 cm^{-1} (circles).

In the next section the density-matrix model is employed in order to describe the interaction of O atoms with very high laser fields ($I > 1 GW/cm^2$).

4. Density-matrix regime

When a ns-laser is strongly focused (e.g. beam diameter ~ 10 μm) the instantaneous intensity *I(t),* can reach more than 100 GW/cm^2 even for lasers with energy of 1 mJ per pulse. In this case the main loss channel of the excited state is the ionization channel. This because the rate of this process largely overpasses the quenching rate. Beside the saturation regime that is rapidly reached, the time-dependent Stark shifts of eigen states are important. As result, the transition energy is detuned, and the two-photon absorption probability is changed. In addition, coherent excitation processes become important and lead to Rabi oscillations. The probability density of populations in ground and excited states oscillates in time. Therefore, the time-resolved fluorescence signal oscillates as well. In this regime the dynamics of the system is described by density-matrix equations [28].

Most of the TALIF plasma diagnostic experiments use ns-pulsed linear polarized lasers that are generally multimode with stochastic phase fluctuation. The decoherence processes such as quenching, Doppler effect and the random phase fluctuation of laser modes will destroy Rabi oscillations [28][52][53]. In this case population dynamics can be described by the set of rate equations with time dependent rates. However, even for large quenching rates at atmospheric pressure, the Rabi regime is reached by focusing the ns-lasers with short optics.

The commercial ns-lasers are linear polarized and have typical spectral width between 0.1 $cm^{-1}$to a few cm^{-1}. The energy separation of the fine structure of O in the ground state ($^3P_{J=2,1,0}$ at energies 0 cm^{-1} (J=2), 159 cm^{-1} (J=1), and 227 cm^{-1} (J=0)) is outside of the laser width. So, only one of the ground state components is excited. The energy separation of the fine structure of upper state ($^3P_{j=2,1,0}$) is less than 1 cm^{-1} (J=1: 88630.587 cm^{-1}, J=2: 88631.146 cm^{-1}, J=0: 88631.303 cm^{-1}; see NIST [7]), therefore this is often unresolved as shown in figure 2a, and different components are simultaneously excited. However, using a linear polarized laser only transitions for $\Delta M_J=0$ can be excited. Transitions from a given M_{J0} will form an independent channel for the two-photon absorption. For each M_{J0} channel the density matrix equation system needs to be solved. Starting from the ground state $J_0=2$ we have to solve five systems of equations for transitions from $M_{J0}=0,\pm1,\pm2$. Due to the section rules the maximum number of the intermediate states for one channel of $2p^4(^3P_2)\rightarrow 2p^3$ (n=3)($^3P_{0,1,2}$) are two.

Using the results published by Dixit et al. [54], the density-matrix equations governing the four-level system can be adapted to our three-level system (ground plus two intermediate eigen states) in which we can add loss of the population and coherence by the collisional quenching at atmospheric pressures:

$$\frac{d\rho_{00}}{dt}=-\frac{i}{2}\left(\Omega_{01}\rho_{10}-c.c.\right)-\frac{i}{2}\left(\Omega_{02}\rho_{20}-c.c.\right) \tag{7a}$$

$$\frac{d\rho_{11}}{dt}=-(\gamma_N+\Gamma_1+\gamma_Q)\rho_{11}+\frac{i}{2}\left(\Omega_{01}\rho_{10}-c.c.\right)+\frac{i}{2}\left(\Omega_{12}^{*}\rho_{12}-c.c.\right) \tag{7b}$$

$$\frac{d\rho_{22}}{dt}=-\left(\gamma_N+\Gamma_2+\gamma_Q\right)\rho_{22}+\frac{i}{2}\left(\Omega_{02}\rho_{20}-c.c.\right)+\frac{i}{2}\left(\Omega_{21}^{*}\rho_{21}-c.c.\right) \tag{7c}$$

$$\frac{d\rho_{10}}{dt}=-\left[\frac{\gamma_N+\Gamma_1+\gamma_Q}{2}-i\Delta_1\right]\rho_{10}+\frac{i}{2}\Omega_{10}\left(\rho_{11}-\rho_{00}\right)-\frac{i}{2}\Omega_{12}\rho_{20}+\frac{i}{2}\Omega_{20}\rho_{12} \tag{7d}$$

$$\frac{d\rho_{20}}{dt}=-\left[\frac{\gamma_N+\Gamma_2+\gamma_Q}{2}-i\Delta_2\right]\rho_{20}+\frac{i}{2}\Omega_{20}\left(\rho_{22}-\rho_{00}\right)-\frac{i}{2}\Omega_{21}\rho_{10}+\frac{i}{2}\Omega_{10}\rho_{21} \tag{7e}$$

$$\frac{d\rho_{12}}{dt}=-\left[\gamma_N+\frac{\Gamma_1+\Gamma_2}{2}+\gamma_Q+i\left(\omega_{12}+S_{12}\right)\right]\rho_{12}-\frac{i}{2}\Omega_{10}\rho_{02}+\frac{i}{2}\Omega_{02}\rho_{10}+\frac{i}{2}\left(\Omega_{12}^{*}\rho_{11}-\Omega_{12}\rho_{22}\right) \tag{7f}$$

Where Ω_{01} and Ω_{02} represents the Rabi frequencies from the ground state to the resonant state, γ_N and γ_Q are the natural and the quenching width and are considered the same for the intermediate states. Γ_1 and Γ_2 are the ionization width out of the resonant states. Δ_1 and Δ_2 are the detunings of the two-photons from the Stark shifted energy difference between the ground

and the resonant states: $\Delta_{1,2} = 2\omega_L - (\omega_{1,2} - \omega_0) - (S_{1,2} - S_0)$. S_i represents the time-dependent Stark shift of the state $|i\rangle$, $\omega_{i=0,1,2}$ represents the energy of the state $|i\rangle$, ω_L represents laser frequency, $\omega_{12} = \omega_1 - \omega_2$ and $S_{12} = S_1 - S_2$. Ω_{12} and Ω_{21} are equal and describe the interference between the ionization channels. For example, in case of the channel M_{J0}=0, intermediate state J=0 and for intensity I = 1 GWcm^{-2}, with data from [54] we compute Ω_{01}=1.86 Hz W^{-1}cm^2 x I = 1.86 GHz, Γ_1 = 0.471 Hz W^{-1}cm^2 x I =0.471 GHz and S_1= 6.51 Hz W^{-1}cm^2 x I= 6.51 GHz, for Rabi, ionization and Stark frequencies, respectively.

The diagonal terms of the density-matrix (i.e. ρ_{00}, ρ_{11} and ρ_{22}) are the density probability of populations in the ground and resonant excited states. The off-diagonal terms (i.e. ρ_{10}, ρ_{20} and ρ_{12}) are the so-called coherences. The excited state probability is calculated for each $|J_0,M_{J0}\rangle$ channel (based on the time evolution of the ρ_{11} and ρ_{22}) and is then averaged over the initial M_{J0} levels.

Even at atmospheric pressure, the quenching width is relatively small compared to the laser width of the commercially available lasers. Therefore, the effect of the laser width on the excitation probability needs to be considered. If the laser line shape arises from stochastic phase fluctuation and its spectrum is a Lorentzian with FWHM γ_L, it can be introduced in 7d and 7e equations as terms of $\gamma_L\left(\beta^2/\Delta_{1,2}^2 + \beta^2\right)$, where the spectral cutoff $\beta >> \gamma_L$ [55]. This term participates in the coherence decay and will contribute to the so-called transverse relaxation time.

In figure 14 a, b simulations of the excited state probability were carried out using the rate equations (1) and the matrix-density equations (7), for an applied constant laser pulse of 10-ns and for different laser intensities. For simplicity, the laser was considered in both cases Lorentzian. The two-photon absorption spectral profile was considered dominated by the laser broadening, with FWHM equal to 1 cm^{-1}, $G^{(2)}(0)$=1, the quenching rate Q=10^{10}Hz and $\beta=10\times\gamma_L$. In both simulations the probability was calculated considering a unresolved fine structure of the upper level.

A first interesting result is the near identical time evolution of the excited state population probability (differences below 5%) obtained by rate equations and by density matrix equations for intensity at 100 MWcm^{-2}. At 1 GWcm^{-2} the saturation effects are shown by the decay of the excited state probability, the difference is below 30 %. For simulations at 10 GWcm^{-2} and 100 GWcm^{-2} the Stark detuning and the coherent excitation are very important. For these intensities the rate equations are obviously not valid. Probabilities are significantly

different and Rabi oscillations can be clearly observed at 100 GWcm^{-2} for the time window of about 100 ps.

Excited state probability

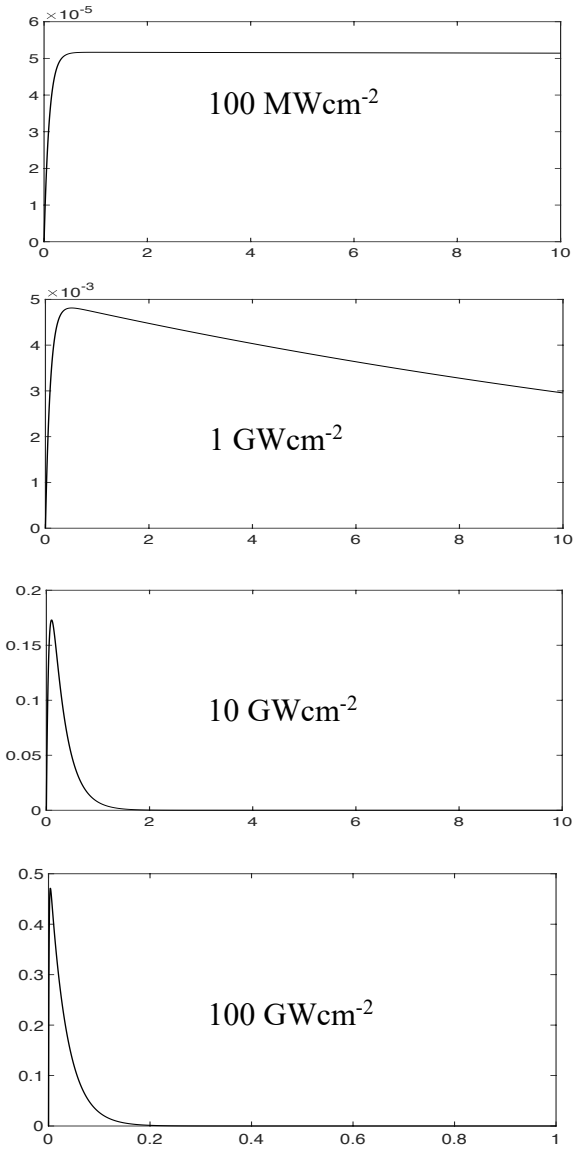

Figure 14a. Excited state probability function of time using rate equations.

Excited state probability

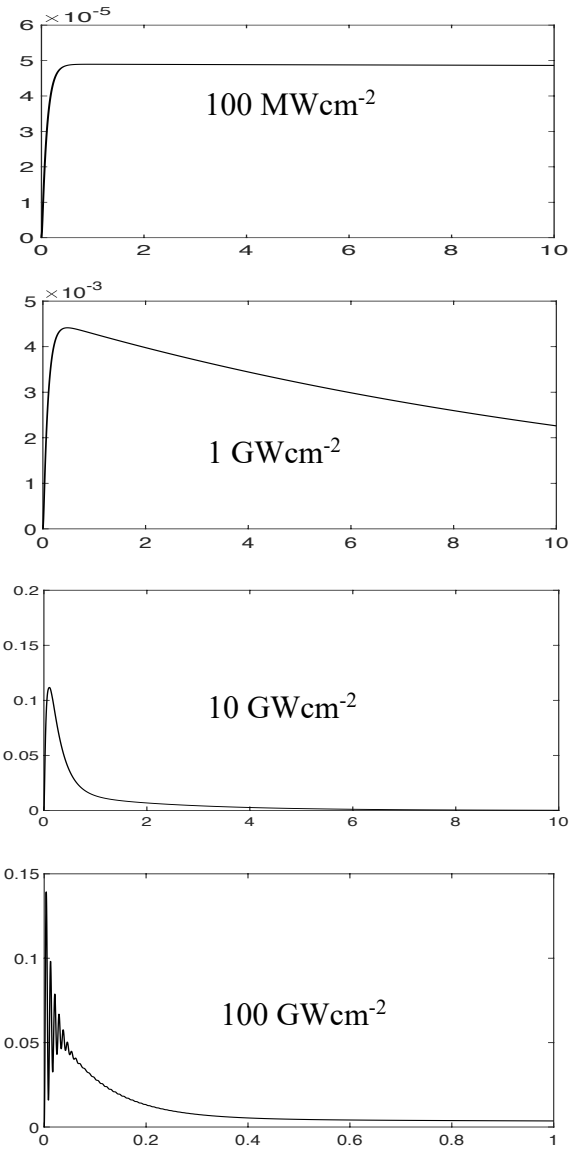

Figure 14b. Excited state probability function of time using density-matrix equations.

As discussed by Eagels et al. [53] the density matrix equations reduce to a set of rate equations when the $\gamma_L + \gamma_a >> \Omega^{(2)}(t), 1/\tau_L$, where γ_L is the laser width, γ_a is the width of the resonant excited state, which includes the natural, the Doppler and collisional widths, $\Omega^{(2)}(t)$ is the composite Rabi frequency and τ_L is the laser pulse length.

Indeed at 100 MWcm^{-2} the composite Rabi frequency for O computed using data from [54] gives an averaged value of $\Omega^{(2)} \sim 5\text{x}10^{10}$Hz for the five independent channels. The reciprocal laser pulse width is $1/\tau_L \sim 10^8$Hz. Both values are much smaller than the laser width, i.e. ~$2\text{x}10^{11}$Hz.

The fluorescence probability is proportional with the time integral of the excited state probability. This is computed by Eq (2). From figure 14 b the highest fluorescence probability for 10 ns laser pulse (fluorescence ~ area under the curve), is obtained for the curve at 10 GWcm^{-2}. This optimum occurs because at even higher intensities the population of the coupled ground and excited states are significantly lost by ionization processes.

Note that the validity of rate equations for intensities up to 1 GWcm^{-2} (as shown in above simulations) is restricted to lower intensities, when spectrally narrower ns-laser are employed (e.g. 0.1 cm^{-1}) or in case of partially mode-locked lasers (e.g. $G^{(2)}(0) > 2$).

Another interesting question to address with density matrix equations is the probability of the excited state as a function of the quenching rate for different laser intensities. In figure 15 a, b simulations were performed for negligible quenching (i.e. Q = 10^5) and for Q=10^{10} Hz, which can be reached in atmospheric or high-pressure plasmas. At 1 GWcm^{-2} for negligible quenching, the fluorescence probability for the 10 ns laser pulse (which is proportional to area under the curve) is more than one order of magnitude higher. This difference reduces within a factor 4 at 10 GWcm^{-2}. Whereas for 100 GWcm^{-2} near identical evolutions of the excited state is shown and the fluorescence probability ratio gives $\left(\int_0^{10ns} A_{21} n_2(t)\,dt\right)_{Q=10^{10}} \Big/ \left(\int_0^{10ns} A_{21} n_2(t)\,dt\right)_{Q<10^6} = 0.66$. The ionization rate ($\Gamma \approx 6\times10^{10}\,Hz$) is significantly larger than the quenching rate ($Q = 10^{10}\,Hz$). Thus, the O-TALIF is practically a quench-free technique when the laser intensity reaches 100 GWcm^{-2}. The fluorescence probabilities during the laser pulse, i.e. $\int_0^{10ns} A_{21} n_2(t)\,dt$, for Q: 10^5, 10^9 and 10^{10} Hz are in ratios of 1 : 0.95 : 0.66, respectively. Thus, for I ~ 100 GWcm^{-2} in atmospheric pressure plasmas, for the typical spatial and temporal changes of Q (i.e. 10^9 Hz to 10^{10} Hz), the TALIF detection becomes nearly unaffected by quenching processes.

Errors due to quenching are here comparable with the spectroscopic errors (< 40 %). Note that the fluorescence computed after the laser pulse, i.e. $\int_{10ns}^{\infty} A_{21} n_2(t)\,dt$, for quenching rates 10^9Hz and 10^{10}Hz is negligible (less than 3%) compared to the fluorescence probability computed for 10 ns duration. We should note also that for a narrower laser (e.g. 0.1 cm^{-1} at 100 GWcm^{-}

^{2}) fluorescence probabilities will converge even better to the same value. Thus, large quenching variations in high pressure plasmas will not change fluorescence signals, and therefore TALIF technique becomes a quench-free oxygen detection method.

This is an important result particularly for non-uniform transient plasmas at atmospheric or high pressures, where quenching can vary drastically in time and space due to changes of the temperature and the nature of colliders. Note that TALIF employed in the non-depletion regime would require a large number of experiments for the quenching characterization, which is not needed in this high intensity regime.

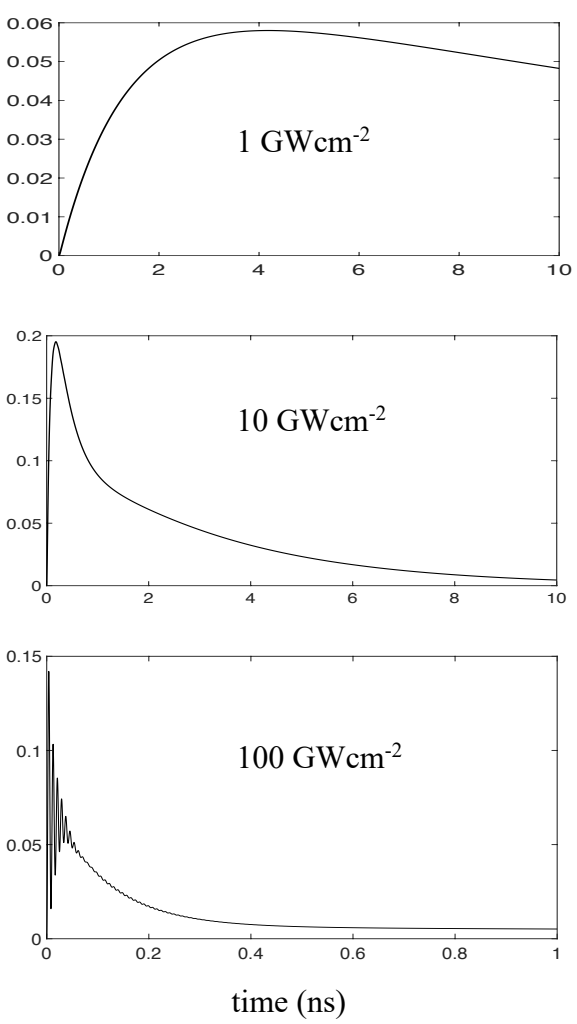

Figure 15a. Excited state probability function of time for negligible quenching.

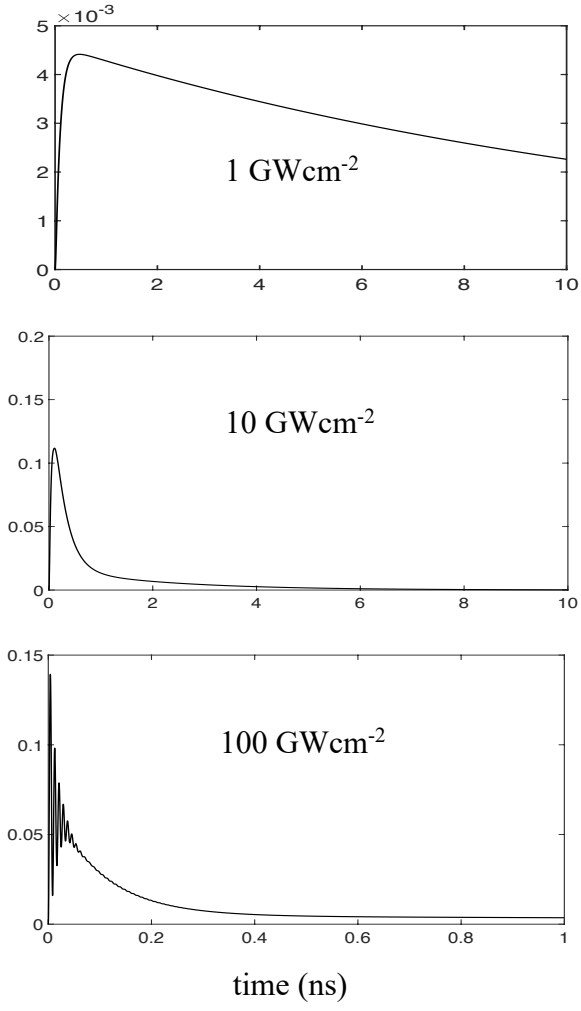

Figure 15b. Excited state probability function of time for Q=10^{10}Hz.

For further developments of the quench-free ns-TALIF technique, experimental results at I ~ 100 GWcm^{-2} should be compared with density-matrix calculations. Careful analysis should be conducted, as the plasma perturbation is additionally enhanced by photon processes (e.g.

photolysis, photoionization, photodetachment). A direct comparison may be performed in case of uniform beams (e.g. shaped using spatial filters) and by ensuring a negligible effect on TALIF signals due to photodissociation and photoelectron induced processes (e.g. ensure the electron quenching rate below 10^{10} Hz).

Finally, it should be noted that in case of a Gaussian beam, averaging over the spatial variation of the laser intensity and the volume would smooth out partially the probability oscillations and will cause the averaged probability to increase slightly beyond the saturation intensity.

5. TALIF plasma diagnostic recommendations

5.1. Two-photon cross-sections for radicals: O, N and H

Regarding the oxygen atom detection, the two-photon absorption transition used by the plasma diagnostic community [35][36][37] is at 225.58 nm ($^3P_2 \rightarrow {}^3P_{2,1,0}$). Its cross-section was theoretically determined in references [56][57][58][54] and experimentally measured in the reference [29]. All theoretical cross-sections were found in excellent agreement (i.e. 1.32, 1.09, 1.03, 1.20 x 10^{-35}cm^4) with the experimental value (i.e. 1.33×10^{-35}cm^4), within the experimental error ± 30%.

Concerning the nitrogen atom, a two-photon transition frequently used by plasma community [36] is at 206.65 nm ($^4S°_{3/2} \rightarrow {}^4S°_{3/2}$). The theoretical paper of K. Omidvar [57] published in 1984, gives 1.37 x 10^{-36} cm^4 for its cross-section. Another two-photon transition also often employed to probe N atoms is at 210.72 nm ($^4S°_{3/2} \rightarrow {}^4D°_{7/2}$). Bischel et al. [59] measured the ratio of this transition to O transition at 225.58 nm ($^3P_2 \rightarrow {}^3P_{2,1,0}$) to be 0.5 (±0.125). This is found in excellent agreement with the theoretical ratio of 0.49 given in reference [57]. We should note also that for O transition at 225.58 nm ($^3P_2 \rightarrow {}^3P_{2,1,0}$), K. Omidvar obtained 1.09x10^{-35} cm^4, which is in very good agreement with the experimental work of Bamford et al. [29] published later in 1986.

The two-photon transition used usually by plasma community to probe H atoms [36] is at 205.08 nm (1s $^2S_{1/2} \rightarrow$3d $^2D_{3/2,5/2}$). In 1971, Gontier et al. [60] and in 1986, Tung et al. [61], obtained the same theoretically value for this transition, namely 1.77x10^{-35} cm^4. There is also a second two-photon transition channel (1s $^2S_{1/2} \rightarrow$3s $^2S_{1/2}$) which is excited at very close wavelength. However, the two-photon cross-section is much smaller and Einstein coefficients for fluorescence channels starting from 3s $^2S_{1/2}$ are also much smaller than those from 3d $^4D_{3/2,5/2}$. Because the ratio of fluorescence intensities induced by the two channels is about

77.5 (a factor 7.56 from the ratio of cross-sections [60], [61] and about ten from the ratio of Einstein coefficients [7]), we can practically neglect the second channel contribution. In 2000, an experimental value was obtained by Bickel et al. [62] for the transition at 243.13 nm ($1s^2S_{1/2} \rightarrow 2s^2S_{1/2}$). Their converted cross-section gives 1.4(±0.4) x 10^{-35} cm^4. The corresponding theoretical value from [60] and [61] is 2.25 x 10^{-35} cm^4. This is again a good agreement if one considers experimental uncertainties and the assumption the authors made on their laser photon statistics.

In table 1, the key spectroscopic properties for the two-photon transitions for O, N and H detection are given. The two-photon cross-sections taken from literature were converted to integrated values using $\sigma^{(2)} = \int \sigma^{(2)}(\omega) d\omega$ (units cm^4, ω is angular frequency). They are appropriate for absorptions performed using one laser beam which is linear polarized. Transition wavelengths (in air) and Einstein coefficients are taken from NIST [7]. Spectral two-photon cross-sections are calculated for the laser tuned at the absorption peak and assuming the Doppler broadening at 300 K and the Gaussian laser with FWHM of 0.1 cm^{-1} ($\sigma^{(2)}(\nu)^*$) and 1 cm^{-1} ($\sigma^{(2)}(\nu)^{**}$).

species	**O**	**N**	**N**	**H**
excited state	$3p[^3P_{2,1,0}]$	$3p[^4D^\circ_{7/2}]$	$3p[^4S^\circ_{3/2}]$	$3d[^2D_{3/2,5/2}]$
two-photon (nm)	225.58	210.72	206.65	205.08
$\sigma^{(2)}$ (cm^4)	1.33(0.4) x 10^{-35} [29]	5.3 x 10^{-36} [57]	1.37 x 10^{-36} [57]	1.77 x 10^{-35} [61]
$\sigma^{(2)}(\nu)^*$ (cm^4s)	1.63 x 10^{-46}	7.66 x 10^{-47}	1.95 x 10^{-47}	7.26 x 10^{-47}
$\sigma^{(2)}(\nu)^{**}$ (cm^4s)	4.6 x 10^{-47}	1.82 x 10^{-47}	4.71 x 10^{-48}	4.75 x 10^{-47}
fluorescence (nm)	844.62; 844.64; 844.68 [a]	868.03	746.83	656.27; 656.29; 656.285[b]
A (Hz)	3.22 x 10^7	2.64 x 10^7	4.16 x 10^7	6.47 x 10^7
A_{21} (Hz)	3.22 x 10^7	2.53 x 10^7	1.96 x 10^7	6.47 x 10^7

Table 1. Spectroscopic data for TALIF O, N and H. All cross-sections do not include $G^{(2)}(0)$ factor; (*) and (**) are computed at peak for Doppler at 300 K, laser width 0.1 cm^{-1} and 1 cm^{-1}, respectively; ([a]) all three transitions occur when using broad lasers (e.g. 1 cm^{-1}); ([b]) fluorescence channels for H are considered unresolved.

As we discussed in previous sections, an accurate TALIF experiment that benefits from the precision of the so-called spectroscopic method (i.e. better than ± 40% for O atoms) requires to be in the non-depletion regime (i.e. low laser intensity). For O atoms from figure 12 and 13, we see that the non-depletion regime is attained when the laser intensity is below 20 MW/cm^2, and this whatever quenching rates between 10^5Hz to 10^{10}Hz (plasmas from low to

atmospheric pressure) and whatever laser widths between 0.1 cm^{-1} to 2 cm^{-1} (typical widths for ns-lasers). In case of atmospheric or high-pressure plasmas where the quenching rate can reach 10^{10}Hz, the non-depletion regime is extended up to about 300 MW/cm^2.

As shown in table 1, line 5, when using a laser of 0.1 cm^{-1}, the atomic oxygen has the largest spectral cross-section among the three species. However, when transitions are excited with broader lasers such as 1 cm^{-1}, O and H peak cross-sections are about the same. Therefore, we expect the hydrogen saturation to become important at approximately the same laser intensity as for oxygen. Yet, the N cross-section for the 206.65 nm is one order of magnitude lower. Because R_{02} scales with I^2, the saturation will roughly occur at laser intensities higher by a factor about three. Consequently, the non-depletion conditions that are valid for O atoms, are also satisfied for H and N atoms.

5.2. Calibration schemes using Xe and Kr

Calibration schemes using Xe and Kr, were proposed in 1998 by Goehlich et al. [35] and in 2001 and 2005 by Niemi et al. [36], [37]. Because two-photon absorption cross-sections were not available for Xe and Kr transitions employed in the calibration schemes, the authors have determined the ratios of two-photon cross-sections. For this purpose, they have used calibration cells filled with known density of Xe and Kr (assuming ideal gas law), titration methods to determine the absolute densities of O, N, and H radicals and the well-known O cross-section value taken from [29]. Fluorescence intensities were compared, and based on Eq (5) the ratio of two-photon cross-sections were obtained by Niemi et al. [36] as: $\sigma^{(2)}_{204.13nm}(Kr)/\sigma^{(2)}_{205.08nm}(H)=0.62$, $\sigma^{(2)}_{204.13nm}(Kr)/\sigma^{(2)}_{206.65nm}(N)=0.67$, $\sigma^{(2)}_{225.44nm}(Xe)/\sigma^{(2)}_{225.58nm}(O)=0.36$, and from Goechlich et al. [35] as: $\sigma^{(2)}_{225.44nm}(Xe)/\sigma^{(2)}_{225.58nm}(O)=0.51$, with an accuracy of 50 %. The Kr and Xe two-photon transitions were at 204.13 nm and 225.44 nm, respectively. In 2005, Niemi et al. [37] proposed a better calibration scheme for oxygen detection, using Xe with two-photon and fluorescence transitions at 224.3 nm and 834.9 nm, respectively. The two-photon cross-section ratio obtained from their measurement was $\sigma^{(2)}_{224.3nm}(Xe)/\sigma^{(2)}_{225.58nm}(O)=1.9$, with an accuracy of 20 %.

From these experimental ratios we can deduce that $\sigma^{(2)}_{205.08nm}(H)/\sigma^{(2)}_{206.65nm}(N)=0.67/0.62=1.08$, for the two-photon transitions of H at 205.08 nm and N at 206.65 nm, respectively. Yet, this is in large disagreement with the theoretical ratio, which is found more than one order of magnitude bigger, namely $\sigma^{(2)}_{205.08nm}(H)/\sigma^{(2)}_{206.65nm}(N)=1.77\times10^{-35}/1.37\times10^{-36}=12.92$.

The theoretical cross-sections for N and H are given without uncertainty values in [57],[60],[61]. However, the precision of theoretical cross-sections can be judged from the very good agreements with spectroscopic experiments. We should recall that experimental and theoretical cross-section ratios of N (210.72 nm) and O (225.58 nm) are in excellent agreement (i.e. 0.5(±0.125) [59] and 0.49 [57]), and all theoretical values cited in section 5.1 for O (225.58 nm) and H (243.13 nm) are in very good agreement with the experimental cross-sections (all within less than factor 1.6).

Experiments from Goechlich et al. [35], and Niemi et al. [36], [37] appear also fairly accurate. The non-depletion regime was checked by plotting fluorescence intensities (I_{LIF}) function of the laser squared energy (E^2_{pulse}). When we compute for O, H, Kr and Xe experiments $\ln\left(I_{LIF(1)}/I_{LIF(2)}\right)/\ln\left(\sqrt{E^2_{pulse(1)}}/\sqrt{E^2_{pulse(2)}}\right)$, slopes in the range of 1.9 to 2.1 are obtained from their data. As these slopes are close to 2, we may consider Eq (5) to be valid. However, this is not entirely accurate. In practice, we will need to satisfy the two criteria, namely *(i)* $\tau_L R_{02} << 1$ and *(ii)* $R_{20} + \Gamma << A + Q$, and to ensure negligible photolytic effect in case of molecular experiments.

Unfortunately, we cannot verify the validity of criteria mentioned above. The laser intensity (or the beam diameter) at the fluorescence collection point is not given in these publications. As shown in figure 12, the laser intensity value (units W/cm^2) determines non-depletion or saturation regimes, and as discussed in section 3.3, it allows to estimate the photolytic effects. Another critical point is the employment of spectral filters and photomultipliers to detect fluorescence signals instead of spectrometers. The recorded signals may contain background emissions of different natures and percentages. For instance, as shown in figure 6, in a Xe gas cell even at low pressure an additional line of about 30 % intensity compared to fluorescence line is recorded at only 6 nm spectral distance. This line can be well in the spectral window of interference filters of 10-nm or 19-nm FWHM, as those used in [35], [36], [37]. In addition, the background signal due to straylight can be important (see figure 6) and need to be subtracted. This issue is also present for radicals detected in the gas-flow system. For detection in plasmas, besides additional atomic or molecular spectral features and the straylight, the continuum background radiation due to recombination or bremsstrahlung may be significant in the spectral window of the filter.

These types of contributions cannot be accurately subtracted from fluorescence signals measured using the detection systems from [35], [36], [37]. The spectral overlapping is

suggested by the systematic overestimation of radiative lifetimes that are between 10% to 80% larger than in NIST [7]. In [35] the Xe(7p[3/2]$_2$) radiative lifetime is measured to be 123 ns, whereas NIST gives about 106 ns. In table 1 of [36],[37] the radiative lifetime of excited states O(3p[^{3}P$_{2,1,0}$]), H(3d[^{2}D$_{3/2,5/2}$]), N(3p[^{4}S$^\circ_{3/2}$]), Kr(5p'[3/2]$_2$ and Xe(6p'[3/2]$_2$ were measured as: 35.1, 17.6, 29.6, 34.1, and 40.8 ns, respectively. If we compute radiative lifetimes using the reciprocal of the sum of Einstein coefficients recommended by NIST we get: 31.1, 15.46, 24.04, 28.5 and 22.81 ns, respectively.

Using a similar approach and detection system, Boogaards et al. [63] reported in 2002 a value of 0.56 for the cross-section ratio of Kr and H, which is close to 0.62 given in [36]. However, this result is also susceptible of systematic errors due to issues mentioned above.

Thus, the disagreement between the theoretical and the experimental two-photon cross-section ratios originates probably from larger uncertainties of experiments performed in [35], [36], [37]. Therefore, calibration schemes and cross-section ratios using rare gases should be reassessed. Here, we should mention the recent work of Drag et al. [64] published in 2019, where Xe (6p'[3/2]$_2$) two-photon absorption cross-section was determined using a direct absorption technique in a reference gas cell. The authors reported a value lower by a factor 2 than that given in [37]. Note that this approach eliminates most of problems related to the quantitative TALIF and therefore a superior accuracy is expected.

5.3. TALIF using ultrafast lasers

When employing ultrafast lasers such as 100-fs that are mode-locked lasers with negligible phase fluctuation, the two-photon transitions are expected to be coherent processes. This because the laser excitation lasts much shorter time than the collision time and consequently decoherence processes due to quenching are negligible. Natural and Doppler decoherence processes are also unimportant during the laser interaction time. The characteristic times of quenching (≥ 100 ps), of Doppler (for O at room temperature ~ 20 ps) and of natural (for O excited states ~ 30 ns) decoherence processes are much larger than the excitation time (~ 100 fs). This suggests that density matrix equations cannot be reduced to rate equations. Yet, in the literature calibrations using rare gases based on Eq (5) are performed, which implies not only the validity of the rate model but also the non-depletion condition. An accurate quantitative approach should take into account the coherent excitation. The $G^{(2)}(0)$ factor for mode-locked lasers is a very large number, which approaches $G^{(2)}(0) \approx 1/3\left[2N + 1/N\right]$ [65], where N are the number of locked modes (e.g. on the order of 10^5 for a fs-laser). Thus, the sensitivity is largely increased when using fs and ps lasers. Note that a commercial 100-fs

laser has energy per pulse in UV (e.g. 205 nm) on the order of tens of μJ. The instantaneous intensity can reach PWcm^{-2} if the laser is strongly focused (beam diameter ~ 10 μm). Therefore, the Stark detuning of transition components needs to be considered. For radicals and rare gases detuning phenomena have different strengths. Due to the large spectral width (e.g. 100-fs laser at Fourier limit gives about 146 cm^{-1} spectral width), the excitation of many transitions and species at the same time should also be evaluated.

Another key advantage when employing ps- and fs-TALIF is the reduced photolytic effect [25] [26]. This can be easily understood if we inspect the criterion for the photolytic-free regime. For example, in case of the molecular oxygen photolysis, this reads $2\sigma_{O_2}^{ph}\left(I/h\nu\right)\tau_L\left(n_{O_2}/n_O\right)<<1$. When using a 100-fs laser, the pulse length (τ_L) is a factor 10^{-5} smaller than for a 10-ns laser. Therefore, as long as the laser intensity ratio (I_{fs} / I_{ns}) is smaller than a factor 10^5, the ultrashort laser fulfils better the photolytic-free criterion.

5.4. Recommendations for TALIF diagnostics

Often in plasma diagnostics articles employing TALIF (or LIF) techniques with nanosecond (or ultrashort) lasers, diagnostic key parameters are only partly evaluated. The validity of Eq (5) is incompletely established by plots of the fluorescence versus the laser pulse energy frequently in arbitrary units instead of the laser intensity units (Wcm^{-2}). As described in previous sections, photolytic combined with saturation effects can mislead the interpretation of these plots. Moreover, even a 1-mJ 10-ns commercial laser can provide very high instantaneous intensities (e.g. 100 GWcm^{-2}), where the fluorescence evaluation requires density-matrix models.

As shown by the excellent work of Bamford et al. [29] on the atomic oxygen, in order to perform accurate measurements, we need to carefully treat all variables impacting the TALIF signal. Note that their experiments were done at 0.5 torr with laser intensities < 16 MWcm^{-2}, for which, as indicated in figures 4 and 12, the depletion and photolytic effects are negligible.

Within less than a factor two (mainly due to the assumption on photon statistics), calibrations using standard radiance sources, Rayleigh or spontaneous Raman scattering based techniques, should be employed. This can significantly reduce error sources that are inherent for Xe or Kr calibration-based techniques. For instance, a calibration using a commercial standard source can have the spectral radiance (W/nm m^2 sr) with a precision of +/-2 %. An accurate spatial filtering and beam profile characterization may increase uncertainties on the order of ten, twenty percent. Whereas, at present, the Xe two-photon absorption cross-section seems to be known with a precision of a factor two. Moreover, at present according to NIST, from nine

spontaneous transitions of the Xe excited state, the Einstein coefficients are given only for three transitions with +/-18 % accuracy. In addition, one should consider also errors of quenching rates, of ionization cross sections and of the rare gas density. Yet, as discussed in section 3.2, the calibration using rare gases has very important advantages and therefore the community should continue to address the accuracy issues.

To summarize, for accurate and sensitive measurements of atomic densities by TALIF using ns-lasers one should check the following items:

- for best sensitivity, use the highest laser energy, employ photon collection systems with large solid angles and detectors with high sensitivity at the fluorescence wavelength,
- when employing spectral filters, check the nature of the collected light using spectrometers,
- to ensure negligible depletion and photolytic effects:
    - measure the laser beam waist in the plasma region where the fluorescence is collected and compute I^2,
    - measure $g(\nu_{peak})$ that is specific for experimental conditions,
    - estimate $G^{(2)}$ for the employed laser type (usually $G^{(2)} \sim 2$ if multimode laser with stochastic phase fluctuation; $G^{(2)} = 1$, for single mode ns laser; this parameter cancels out when calibrations with rare gases are performed),
    - calculate the two-photon absorption rate R_{02} and adjust beam optics in order to satisfy the non-saturation criterion *(i)*: $R_{02}\tau_L << 1$,
    - measure the quenching rate Q from the decay time of the fluorescence signal (it may require ps-lasers at atmospheric pressure),
    - verify the criterion *(ii)*: $R_{20} + \Gamma << (A + Q)$, when invalid, adjust beam optics to satisfy the inequality,
    - estimate the photolytic effect in cases where large concentrations of photolytic sensitive species are present (e.g. $2\sigma_{O_2}^{ph}\left(I/h\nu\right)\tau_L\left(n_{O_2}/n_O\right) << 1$).

Disregarding photon statistics, similar recommendations can also be established for one-photon laser induced fluorescence (LIF) for atomic or molecular plasma diagnostics.

6. Conclusions

The theory of the two-photon absorption laser induced fluorescence using ns-lasers for plasma diagnostics from low to atmospheric pressures, from low to high laser intensities was

revisited. The rate equation regimes including non-depletion and saturation as well as the density-matrix regime were presented for atomic oxygen. The influence of two-photon absorption cross-section, photon statistics, laser spectral profile, quenching and photolytic processes on the TALIF signals was discussed. Density matrix simulations showed that TALIF becomes a quench-free technique for O detection performed using 10-ns lasers with intensity of 100 GWcm^{-2}. The two-photon cross-section ratios of O, N, H, Kr and Xe, based on the literature theoretical and experimental works were analyzed. It was found that experimental ratios used by the plasma community for calibration should have larger uncertainties than given in references [35],[36],[37]. For accurate and sensitive ns-TALIF measurements a list of recommendations was proposed. In case of the employment of ultrashort lasers, characteristic times of decoherence processes were found much longer than the excitation time. This suggested that the fluorescence assessment requires the density-matrix description, which includes coherent excitations and Stark detuning processes.

References

[1] Ju Y and Sun W 2015 Plasma assisted combustion: Dynamics and chemistry *Prog. Energy Combust. Sci.* **48** 21–83

[2] Kawai Y, Chen S, Honda Y, Yamaguchi M, Amano H, Kondo H, Hiramatsu M, Kano H, Yamakawa K, Den S and Hori M 2011 Achieving high-growth-rate in GaN homoepitaxy using high-density nitrogen radical source *Phys. Status Solidi Curr. Top. Solid State Phys.* **8** 2089–91

[3] Hong J, Pancheshnyi S and Tam E 2017 Kinetic modelling of NH3 production in N2-H2 non-equilibrium atmospheric-pressure plasma catalysis Related content Corrigendum: Kinetic modelling of NH3 production in N2-H2 non-equilibrium atmospheric-pressure plasma catalysis *J. Phys. D Appl. Phys* **50** 154005

[4] Butler J E, Mankelevich Y A, Cheesman A, Ma J and Ashfold M N R 2009 Understanding the chemical vapor deposition of diamond: Recent progress *J. Phys. Condens. Matter* **21**

[5] Flamm D L 1990 Mechanisms of silicon etching in fluorine- and chlorine-containing plasmas *Pure Appl. Chem.* **62** 1709–20

[6] Gupta M, Owano T, Baer D and O'Keefe A 2006 Quantitative determination of the O(3P) density via visible cavity-enhanced spectroscopy *Appl. Phys. Lett.* **89** 1–4

[7] https://www.nist.gov/pml/atomic-spectra-database Nist atomic data base

[8] Stancu G D, Janda M, Kaddouri F, Lacoste D A and Laux C O 2010 Time-resolved CRDS measurements of the N2(A3Σu+) density produced by nanosecond discharges in atmospheric pressure nitrogen and air *J. Phys. Chem. A* **114** 201–8

[9] Göppert-Mayer M 1931 Über Elementarakte mit zwei Quantensprüngen *Ann. Phys.* **401** 273–94

[10] Kaiser W and Garrett C G B 1961 Two-photon excitation in CaF2: Eu2+ *Phys. Rev. Lett.* **7** 229–31

[11] Hãnsch T W, Lee S A, Wallenstein R and Wieman C E 1974 Doppler-free two-photon spectroscopy of hydrogen 1S-2S *Phys. Rev. Lett.* **34** 307–9

[12] Bischel W K, Perry B E and Crosley D R 1982 Detection of fluorescence from O and N atoms induced by two-photon absorption *Appl. Opt.* **21** 1419

[13] Lucht R P, Salmon J T, King G B, Sweeney D W and Laurendeau N M 1983 Two-photon-excited fluorescence measurement of hydrogen atoms in flames *Opt. Lett.* **8** 365

[14] Alden M, Westblom U and Goldsmith J E M 1989 Two-photon-excited stimulated emission

from atomic oxygen in flames and cold gases *Opt. Lett.* **14** 305–7
[15] Gray J A, Goldsmith J E M and Trebino R 1993 Detection of atomic hydrogen by two-color laser-induced grating spectroscopy *Opt. Lett.* **18** 444
[16] Dux R, Grützmacher K, De La Rosa M I and Wende B 1995 Absolute determination of local ground-state densities of atomic hydrogen in nonlocal-thermodynamic-equilibrium environments by two-photon polarization spectroscopy *Phys. Rev. E* **51** 1416–27
[17] Czarnetzki U, Miyazaki K, Kajiwara T, Muraoka K, Maeda M and Döbele H F 1994 Comparison of various two-photon excitation schemes for laser-induced fluorescence spectroscopy in atomic hydrogen *J. Opt. Soc. Am. B* **11** 2155
[18] Dilecce G, Vigliotti M and Benedictis S De 2000 A TALIF calibration method for quantitative oxygen atom density measurement in plasma jets *J. Phys. D. Appl. Phys.* **33** L53–6
[19] Mazouffre S, Foissac C, Supiot P, Vankan P, Engeln R, Schram D C and Sadeghi N 2001 Density and temperature of N atoms in the afterglow of a microwave discharge measured by a two-photon laser-induced fluorescence technique *Plasma Sources Sci. Technol.* **10** 168–75
[20] Oda T, Yamashita Y, Takezawa K and Ono R 2006 Oxygen atom behaviour in the nonthermal plasma *Thin Solid Films* **506**–**507** 669–73
[21] Uddi M, Jiang N, Mintusov E, Adamovich I V. and Lempert W R 2009 Atomic oxygen measurements in air and air/fuel nanosecond pulse discharges by two photon laser induced fluorescence *Proc. Combust. Inst.* **32 I** 929–36
[22] Stancu G D, Kaddouri F, Lacoste D A and Laux C O 2010 Atmospheric pressure plasma diagnostics by OES, CRDS and TALIF *J. Phys. D. Appl. Phys.* **43** 124002
[23] Van Gessel A F H, Van Grootel S C and Bruggeman P J 2013 Atomic oxygen TALIF measurements in an atmospheric-pressure microwave plasma jet with in situ xenon calibration *Plasma Sources Sci. Technol.* **22** 055010
[24] Dvořák P, Mrkvičková M, Obrusník A, Kratzer J, Dědina J and Procházka V 2017 Fluorescence measurement of atomic oxygen concentration in a dielectric barrier discharge *Plasma Sources Sci. Technol.* **26** 065020
[25] Frank J H, Chen X, Patterson B D and Settersten T B 2004 Comparison of nanosecond and picosecond excitation for two-photon laser-induced fluorescence imaging of atomic oxygen in flames *Appl. Opt.* **43** 2588–97
[26] Kulatilaka W D, Gord J R, Katta V R and Roy S 2012 Photolytic-interference-free, femtosecond two-photon fluorescence imaging of atomic hydrogen *Opt. Lett.* **37** 3051
[27] Schmidt J B, Roy S, Kulatilaka W D, Shkurenkov I, Adamovich I V., Lempert W R and Gord J R 2017 Femtosecond, two-photon-absorption, laser-induced-fluorescence (fs-TALIF) imaging of atomic hydrogen and oxygen in non-equilibrium plasmas *J. Phys. D. Appl. Phys.* **50** 015204
[28] Demtröder W 2003 *Laser spectroscopy* (Berlin: Springer-Verlag)
[29] Bamford D J, Jusinski L E and Bischel W K 1986 Absolute two-photon absorption and three-photon ionization cross sections for atomic oxygen *Phys. Rev. A* **34** 185–98
[30] Loudon R 1983 *The quantum theory of light* (Oxford: Clarendon)
[31] Kröll S, Aldén M, Bengtsson P-E, Löfström C and Hall R J 1991 Statistics of multimode YAG laser radiation with implications for quantitative coherent anti-Stokes Raman scattering spectroscopy in combustion diagnostics *J. Opt. Soc. Am. B* **8** 930
[32] Stancu G D 2014 *in Spectroscopy and spectroscopic: measurement techniques for aerospace flows* ed D Giordano and Y Babou, ISBN-13 978-2-87516-076-8 (VKI)
[33] Stancu G D, Leroy O, Coche P, Gadonna K, Guerra V, Minea T and Alves L L 2016 Microwave air plasmas in capillaries at low pressure II. Experimental investigation *J. Phys. D. Appl. Phys.* **49** 435202
[34] Bischel W K, Bamford D J and Jusinski L E 1986 Absolute calibration of a fluorescence collection system by Raman scattering in H_2 *Appl. Opt.* **25** 1215
[35] Goehlich A, Kawetzki T and Döbele H F 1998 On absolute calibration with xenon of laser diagnostic methods based on two-photon absorption *J. Chem. Phys.* **108** 9362–70
[36] Niemi K, Schulz-von Der Gathen V and Döbele H F 2001 Absolute calibration of atomic density measurements by laser-induced fluorescence spectroscopy with two-photon excitation *J. Phys. D. Appl. Phys.* **34** 2330–5

[37] Niemi K, Schulz-Von Der Gathen V and Döbele H F 2005 Absolute atomic oxygen density measurements by two-photon absorption laser-induced fluorescence spectroscopy in an RF-excited atmospheric pressure plasma jet *Plasma Sources Sci. Technol.* **14** 375–86
[38] Kulatilaka W D, Frank J H, Patterson B D and Settersten T B 2009 Analysis of 205-nm photolytic production of atomic hydrogen in methane flames *Appl. Phys. B Lasers Opt.* **97** 227–42
[39] Conway J, Gogna G S, Gaman C, Turner M M and Daniels S 2016 Two-photon absorption laser induced fluorescence measurement of atomic oxygen density in an atmospheric pressure air plasma jet *Plasma Sources Sci. Technol.* **25** 45023
[40] Warneck P 1988 *Chemistry of the natural atmosphere* (Academic Press, San Diego)
[41] Matsumi Y and Kawasaki M 2003 Photolysis of Atmospheric Ozone in the Ultraviolet Region *Chem. Rev.* **103** 4767–81
[42] Brouard M, Parker D H and Van De Meerakker S Y T 2014 Taming molecular collisions using electric and magnetic fields *Chem. Soc. Rev.* **43** 7279–94
[43] Agrup S, Ossler F and Aldén M 1995 Measurements of collisional quenching of hydrogen atoms in an atmospheric-pressure hydrogen oxygen flame by picosecond laser-induced fluorescence *Appl. Phys. B Lasers Opt.* **61** 479–87
[44] Ossler F and Larsson J 1996 Measurements of the effective lifetime of O atoms in atmospheric premixed flames *Chem. Phys. Lett.* **250** 287
[45] Dagdigian P J, Forch B E and Miziolek A W 1988 Collisional transfer between and quenching of the 3p 3P and 5P states of the oxygen atom *Chem. Phys. Lett.* **148** 299–308
[46] Dumitrache C, Gallant A, Minesi N, Stepanyan S, Stancu G D and Laux C O 2019 Hydrodynamic regimes induced by nanosecond pulsed discharges in air: Mechanism of vorticity generation *J. Phys. D. Appl. Phys.* **52** 364001
[47] Amorim J, Baravian G, Touzeau M and Jolly J 1994 Two-photon laser induced fluorescence and amplified spontaneous emission atom concentration measurements in O_2 and H_2 discharges *J. Appl. Phys.* **76** 1487–93
[48] Huang Y L and Gordon R J 1992 The effect of amplified spontaneous emission on the measurement of the multiplet state distribution of ground state oxygen atoms *J. Chem. Phys.* **97** 6363–8
[49] Amorim J and Baravian G 2001 The two-photon absorption laser induced stimulated emission as a hydrogen atoms diagnostic tool: Modelling and experiment *Opt. Commun.* **192** 277–86
[50] Piepmeier E H 1972 Theory of laser saturated atomic resonance fluorescence *Spectrochim. Acta Part B At. Spectrosc.* **27** 431–43
[51] Voráč J, Dvořák P, Procházka V, Morávek T and Ráhel J 2015 Dependence of laser-induced fluorescence on exciting-laser power: Partial saturation and laser - Plasma interaction ∗ *EPJ Appl. Phys.* **71** 20812
[52] Allen L, Eagles K A and Stroud C R 1982 The time development of adiabatic two-photon absorption. I. Low intensity regime *J. Phys. B At. Mol. Phys.* **15** 1643–50
[53] Eagles K A, Stroud C R and Allen L 1982 The time development of adiabatic two-photon absorption. II. Rate equation regime *J. Phys. B At. Mol. Phys.* **15** 2021–6
[54] Dixit S N, Levin D A and McKoy B V 1988 Resonant enhanced multiphoton ionization studies in atomic oxygen *Phys. Rev. A* **37** 4220–8
[55] Zoller P and Lambropoulos P 1979 Non-Lorentzian laser lineshapes in intense field-atom interaction *J. Phys. B At. Mol. Phys.* **12** L547
[56] Pindzola M S 1978 Two-photon excitation of atomic oxygen *Phys. Rev. A* **17** 1021–7
[57] Omidvar K 1984 Errata Erratum : Two-photon excitation cross section in light and intermediate Erratum : Exact solution of some discrete stochastic models with chaos *Phys. Rev. A* **30** 2805
[58] Saxon R P and Eichler J 1986 Theoretical calculation of two-photon absorption cross sections in atomic oxygen *Phys. Rev. A* **34** 199–206
[59] Bischel W K, Perry B E, Crosley D R 1981 Two-photon laser-induced fluorescence in oxygen and nitrogen atoms *Chem. Phys. Lett.* **82** 85–8
[60] Gontier Y and Trahin M 1971 On the multiphoton absorption in atomic hydrogen *Phys. Lett. A* **36** 463–4

[61] Tung J H, Tang A Z, Salamo G J and Chan F T 1986 Two-photon absorption of atomic hydrogen from two light beams *J. Opt. Soc. Am. B* **3** 837
[62] Bickel G A and McRae G A 2000 Determination of the 1s-2s two-photon excitation cross-section in atomic hydrogen *Spectrochim. Acta Part B* **55** 57–63
[63] Boogaarts M G H, Mazouffre S, Brinkman G J, Van Der Heijden H W P, Vankan P, Van Der Mullen J A M, Schram D C and Döbele H F 2002 Quantitative two-photon laser-induced fluorescence measurements of atomic hydrogen densities, temperatures, and velocities in an expanding thermal plasma *Rev. Sci. Instrum.* **73** 73
[64] Drag C, Alkhoury J, Jannaud T, Marmuse F and Blondel C 2019 Two-photon excitation cross-section of Xe revisited *Proc. 24th Int. Symp. Plasma Chem.* 550
[65] Mahr H 1975 *in Quantum Electronics: A Tretise* ed H Rabin and C L Tang (Academic New York)